J. Fluid Mech. (1996), *vol.* 309, *pp.* 1–44

Hysteresis in swirling jets

By VLADIMIR SHTERN AND FAZLE HUSSAIN
Department of Mechanical Engineering, University of Houston, Houston, TX 77204-4792, USA

(Received 4 October 1994 and in revised form 16 September 1995)

This paper explains hysteretic transitions in swirling jets and models external flows of vortex suction devices. Toward this goal, the steady rotationally symmetric motion of a viscous incompressible fluid above an infinite conical stream surface of a half-angle θ_c is studied. The flows analysed are generalizations of Long's vortex. They correspond to the conically similar solutions of the Navier–Stokes equations and are characterized by circulation Γ_c given at the surface and axial flow force J_1. Asymptotic analysis and numerical calculations show that four (for $\theta_c \leqslant 90°$) or five (for $\theta_c > 90°$) solutions exist in some range of Γ_c and J_1. The solution branches form hysteresis loops which are related to jump transitions between various flow regimes. Four kinds of jump are found: (i) vortex breakdown which transforms a near-axis jet into a two-cell flow with a reverse flow near the axis and an annular jet fanning out along conical surface $\theta = \theta_s < \theta_c$; (ii) vortex consolidation causing a reversal of (i); (iii) jump flow separation from surface $\theta = \theta_c$; and (iv) jump attachment of the swirling jet to the surface. As Γ_c and/or J_1 decrease, the hysteresis loops disappear through a cusp catastrophe. The physical reasons for the solution non-uniqueness are revealed and the results are discussed in the context of vortex breakdown theories. Vortex breakdown is viewed as a fold catastrophe. Two new striking effects are found: (i) there is a pressure peak of $O(\Gamma_c^2)$ inside the annular swirling jet; and (ii) a consolidated swirling jet forms with a reversed ('anti-rocket') flow force.

CONTENTS

1. Introduction

1.1. *Observations of bi-stability in swirling flows*

Swirling flows in nature and technology have many striking and even enigmatic features that need thorough analysis and interpretation. In addition to the well-known examples of intriguing phenomena such as the Ranque–Hilsch effect and vortex breakdown, several new ones are revealed here: jump separation and attachment of near-surface swirling flows; a strong peak of pressure inside annular swirling jets; and a paradoxical, upstream-directed flow force in a consolidated swirling jet. These intriguing features are not only of intrinsic scientific interest but also very important for technological applications. Perhaps the most problematic feature of swirling flows is their bi- or multi-stability which can lead to abrupt transitions between different states, occurring at the same values of control parameters. Similar bi-stability is observed in tornadoes (Burggraf & Foster 1977; Shtern & Hussain 1993, hereinafter referred to as SH), vortices above delta wings (Schmucker & Gersten 1988) as well as in the inner and outer flow domains of vortex devices (Goldshtik 1990; Spotar' & Terekhov 1987). These abrupt or jump transitions are most dangerous for aircraft because the resultant changes in lift and drag can lead to a loss of flight control. This has been the main practical motivation for numerous studies of vortex breakdown since its discovery by Peckham & Atkinson 1957).

Although not necessarily as dangerous, several highly undesirable sequences of transitions between flow states occur in various vortex devices. Figure 1(*a*) shows a schematic of a 'focused' suction device (Boguslavskii & Ivanskii 1987) to remove hazardous fumes or aerosols generated at a distant spot. Fresh air pumped through guidevane 1 forms swirling outflow 2, turns around near stagnation point 3, collects hazardous fumes from pollution source 4, and is sucked out through axial pipe 5.

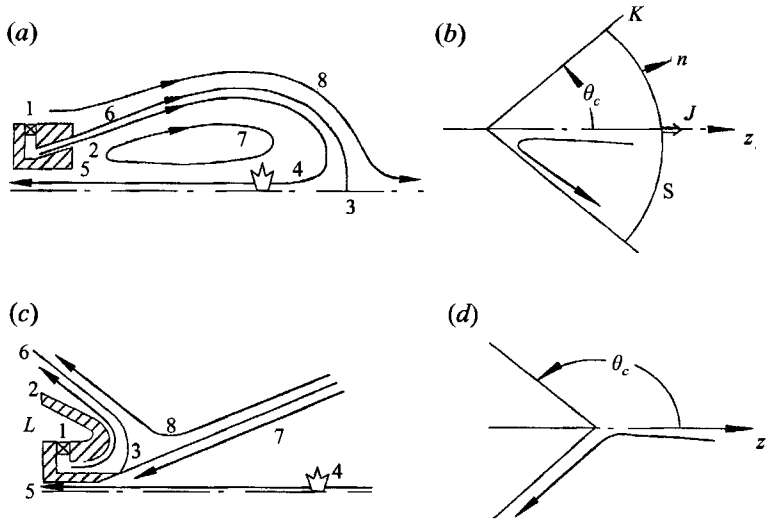

FIGURE 1. Schematic of suction devices (*a*, *c*) and their models (*b*, *d*) with forward (*a*, *b*) and back (*c*, *d*) blowing. (1) Swirling guidevane for pumped fresh air, (2) swirling outflow, (3) stagnation point, (4) source of pollution, (5) orifice for suction of polluted air, (6) separating air screen, (7) typical streamline, (L) Lyahovsky diffuser. Cones $\theta = \theta_c$ model air screen 6, where circulation K is given. Axial flow force J acts on surface S with normal n. Typical streamlines are shown by curves with arrows. The chain line is a symmetry axis.

Stream 6 separates region 7 of circulatory motion from the outer flow 8. The swirling annular jet 6 serves as an air screen that provides a long-range suction effect and prevents dispersal of the fumes. However, a strong enough external disturbance can cause a drastic contraction of the circulatory 'bubble', resulting in the fumes being blown away and dispersed. To avoid this undesirable possibility, a modified device has been invented (Spotar' *et al.* 1994); see figure 1(*c*) in which a new component – Lyahovsky diffuser L – is used to turn back swirling outflow 2 by the Coanda effect and to prevent the bubble contraction.

1.2. *Models of vortex suction devices*

One motivation of this paper is to model external flows of suction devices and to study and predict the jump transitions. For this we simplify the practical flows by modelling a part of separating boundary 6 in figure 1(*a*) by conical stream surface $\theta = \theta_c$ (see figure 1*b*). To model the flow outside the device shown in figure 1(*c*) we increase the included angle θ_c of the cone to correspond with the swirling air screen (figure 1*d*). Therefore, surface $\theta = \theta_c$ is impermeable but not rigid in the model and this is an important point.

In general, the flow similarity and no-slip condition are not compatible when there are no body forces or other motion sources (singularities) inside a flow region. Squire (1952) was the first to discover this; see also Yih *et al.* (1982). The similarity solution with the no-slip coindition is trivial (zero) because there are no motion sources. In the absence of other driving forces, a flow can be driven only by a given non-zero velocity or shear stress at $\theta = \theta_c$. In our model, the swirling jet propagating along surface 6 in figure 1(*a*, *c*) generates the flow in region $\theta \leqslant \theta_c$. Therefore, it would be not physical to use the no-slip condition for stream surface 6. Throughout this paper, 'cone' denotes only a geometric volume of the same fluid, whose surface is fixed and

impenetrable. However, instead specifying the radial velocity or shear stress to be given at $\theta = \theta_c$, the momentum flux is used here as a control characteristic for reasons discussed in the next section.

Thus, the swirling flow inside the cone is considered to be driven by circulation K ($= \nu\Gamma_c$; ν is the kinematic viscosity) given at $\theta = \theta_c$ and axial flow force $J (= 2\pi\rho\nu^2 J_1$; ρ is the density) through cross-section S,

$$J = \int (\rho v_z v_n + p n_z - \tau_{zn})\, \mathrm{d}S,$$

which includes contributions from the momentum flux, pressure p, and viscous stresses. In the model, the only source of axial momentum is at the cone apex, so that J is a flow invariant independent of the shape of S and its location.

If one considers a rigid conical wall and a jet propagating from the apex, such a flow is not described by a similarity solution. Schneider, Zauner & Bohm (1987, also see references therein) studied in detail a swirl-free jet emerging from a hole in a plane wall and showed that there is no similarity. The physical reason is simple: the similarity corresponds to conservation of J but there is a loss of J at the wall. Nevertheless, the similarity can develop in the limiting case as $J_1 \to \infty$ (Schneider 1985). The asymptotic analysis of this paper (§3) shows that the character (slip or no-slip) of the boundary condition at $\theta = \theta_c$ does not influence the result except for flow inside a near-surface shear layer. Therefore, the similarity and no-slip can also be compatible in the limiting case as $\Gamma_c \to \infty$. (Note that ν can be interpreted as constant eddy viscosity of turbulent flows (Long 1961; Serrin 1972). Then $\theta = \theta_c$ may be considered as a rigid wall but with the no-slip condition omitted (Burggraf & Foster 1977; SH). For this reason, the 'inviscid' (slip) condition is used even in the direct numerical simulations of the Navier–Stokes equations to model vortex breakdown in pipes (Beran & Culick 1992; Lopez 1994).) For these reasons, the similarity approach with the slip condition is a useful preliminary stage for more complicated models.

By this idealization we reduce requirements on conditions controlling the external flows of the vortex devices to two parameters, Γ_c and J_1, which characterize the intensities of swirl and blowing respectively. In spite of this strong idealization, the model retains the key elements leading to jump transitions in the devices. This is not particularly surprising because both the outer circulation and the flow force are quantities that are nearly conserved when vortex breakdown or other jumps occur away from rigid walls. This conservation is our main reason for using here the integral quantity J_1 instead of such local characteristics as the radial velocity or stress at $\theta = \theta_c$.

1.3. *Flow force as a control parameter*

The flow force J is a traditional characteristic of jet-like flows based on the conservation of axial momentum flux. For swirl-free round jets, J has been used by Schlichting (1933) under the boundary layer approximation, by Landau (1944) for the exact solution of a jet issuing from a point source of momentum in infinite space, and by Squire (1952) for a jet issuing normal to a plane. The conservation of J results in the fact that these solutions of the boundary layer and the Navier–Stokes equations have conical similarity. That is, the velocity is inversely proportional to distance r from the origin of the jet; such similarity is observed experimentally in turbulent jets (e.g. Hasan & Hussain 1982). A constant value of the outer circulation for swirling jets also agrees with the conical similarity. For rotationally symmetric flows, the use of the conical similarity results in the reduction of the Navier–Stokes equations to a system

of ordinary differential equations (ODE) which considerably simplifies the analysis and permits a detailed parametric investigation. The similarity flows with K and J as control parameters were studied by Long (1961) in the boundary-layer approximation for a near-axis jet with a strong swirl and by Goldshtik (1979) for a few specific solutions of the Navier–Stokes equations with small Γ_c.

Long (1961) introduced $M = J/(\rho K^2)$ as the only asymptotic characteristic of the flow as $\Gamma_c \to \infty$ and found a striking feature: two solutions which exist for $M > M_{*L}$ merge and disappear at $M = M_{*L} = 3.65$, and no solution exists for $M < M_{*L}$. Burggraf & Foster (1977) related this feature (i.e. fold) to vortex breakdown and found the more precise value of $M_{*L} = 3.75$. Because Long's problem is a simple but pithy model of a strong vortex, its different aspects have been studied in a number of subsequent papers (Morton 1969; Foster & Duck 1982; Foster & Smith 1989; Fernandez de la Mora, Fernandez Feria & Barrero 1991; Foster & Jacqmin 1992; Khorami & Triveli 1994). Note that a study of the same conically similar Navier–Stokes equation solutions does not show any fold and non-uniqueness when different control parameters are used (Yih *et al.* 1982; Goldshtik & Shtern 1990). The fold has also been found for Serrin's vortex (Goldshtik & Shtern 1990) and in two more problems related to vortex breakdown in inviscid (Saffman 1992) and viscous (Beran & Culick 1992; Lopez 1994) flows. However, Long's approach seems to be the most appropriate for swirling jets because J and K are conserved during jump transitions. The conservation of J and K is also a key element of the inviscid theory of vortex breakdown by Squire (1956), Benjamin (1962), and Keller (1994, see also references therein). Although in viscous fluid a loss of J and K does take place at rigid boundaries, this loss can be neglected for such an abrupt phenomenon as vortex breakdown. The reason is that the loss occurs inside viscous boundary layers on the remote walls and, therefore, cannot strongly influence the flow region where vortex breakdown occurs. Thus, a generalization of Long's approach to a wider class of the NSE solutions in conical regions seems reasonable and useful; this is another motivation of our paper.

1.4. *Limitations of Long's model*

A serious limitation of Long's (1961) results is the non-existence of solutions for $M < M_{*L}$, although solutions of the Navier–Stokes equations do exist in this range of M. This limitation originates from the consideration of the near-axis boundary layer only. To understand what flows occur for $M < M_{*L}$ and to reveal the hysteretic nature of vortex breakdown, one needs to look for solutions with different flow patterns. For this a wider flow region and the full Navier–Stokes equations must be considered. SH's generalization of Long's problem considers the swirling flow above an impermeable plane, $z = 0$, treating the flow as a model tornado. SH found that an additional fold exists involving vortex consolidation, and there are at least three solutions for the same Γ_c and J_1 in some region of the parameters. For some values of Γ_c and J_1, the flow can be descending with a near-surface jet or two-cellular with a jet fanning out along a conical surface $\theta = \theta_c < 90°$. These flow patterns are outside the scope of Long's approach. Drazin, Banks & Zaturska (1995) also consider the generalization of Long's vortex for the half-space but with a given (non-zero) normal velocity at $z = 0$, in contrast to the impermeability condition used by SH.

This paper considers the entire range of the conical surface angle, $0 < \theta_c < 180°$, while SH considered only $\theta_c = 90°$. Such a generalization, which may superficially appear to be simple, not only covers a very wide range of flows but also reveals striking new features: multi-stability, jump flow separation from and attachment to the cone surface, and a swirling jet with an 'anti-rocket' thrust. The term 'anti-rocket' is used

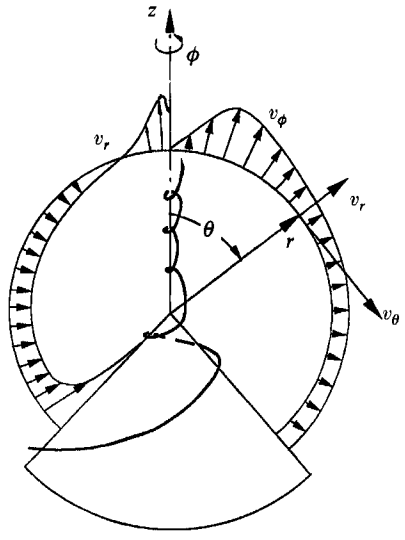

FIGURE 2. Schematic of the problem: a typical streamline (helical curve) and profiles of the radial and swirl velocities for an ascending swirling jet.

to indicate that the jet produces a thrust in the direction of the jet flow, in contrast to the typical oppositely directed thrust in rockets. Figure 2 shows a three-dimensional schematic of the consolidated swirling jet with the anti-rocket thrust. It shows a typical streamline, velocity profiles and spherical coordinates.

Although particular flow features crucially depend on θ_c, there are several common features: more folds and solution branches corresponding to flow patterns distinct from the near-axis jet exist. One can view the flow as a superposition of swirl and meridional motion. Figure 3 shows, for clarity, only the meridional motion of three different flow patterns observed in this problem: (*a*) a consolidated upward swirling jet; (*b*) a two-cell structure with an ascending flow in region 1, a downward near-axis stream in region 2, and an annular jet fanning out near conical surface $\theta = \theta_s$ which separates the two cells; and (*c*) a flow exactly opposite to (*a*). Note that Long's boundary-layer approach addresses only the near-axis region of flow pattern (*a*). Moreover, even in this particular case, the contribution to J_1 from the outer region of the boundary layer is of a higher order of magnitude than that of the near-axis jet when $\Gamma_c \to \infty$. An exception is the particular case, $\theta_c = 90°$, studied by SH, where the two contributions are of the same order of magnitude. It will be shown here that the contribution to J_1 from the outer region can be crucial for vortex devices where the paradoxical anti-rocket thrust occurs. This paper's goal is to overcome the above limitation of Long's approach and to explain hysteretic transitions related to vortex breakdown and consolidation.

1.5. *Hysteresis loops*

Figure 3(*d*) shows a schematic of the hysteresis loops in our problem. J is a (given) control parameter (e.g. the flow force), and V is a parameter found from the solution (say, a characteristic velocity). The upper, middle, and lower branches of the curve in figure 3(*d*) are shown by the solid lines and correspond to patterns (*a*), (*b*), and (*c*) in figure 3, respectively. The dashed branches in figure 3(*d*) denote regimes which presumably cannot be observed in experiments owing to their instability. Arrows indicate unavoidable jump transitions between the regimes: vortex breakdown (B),

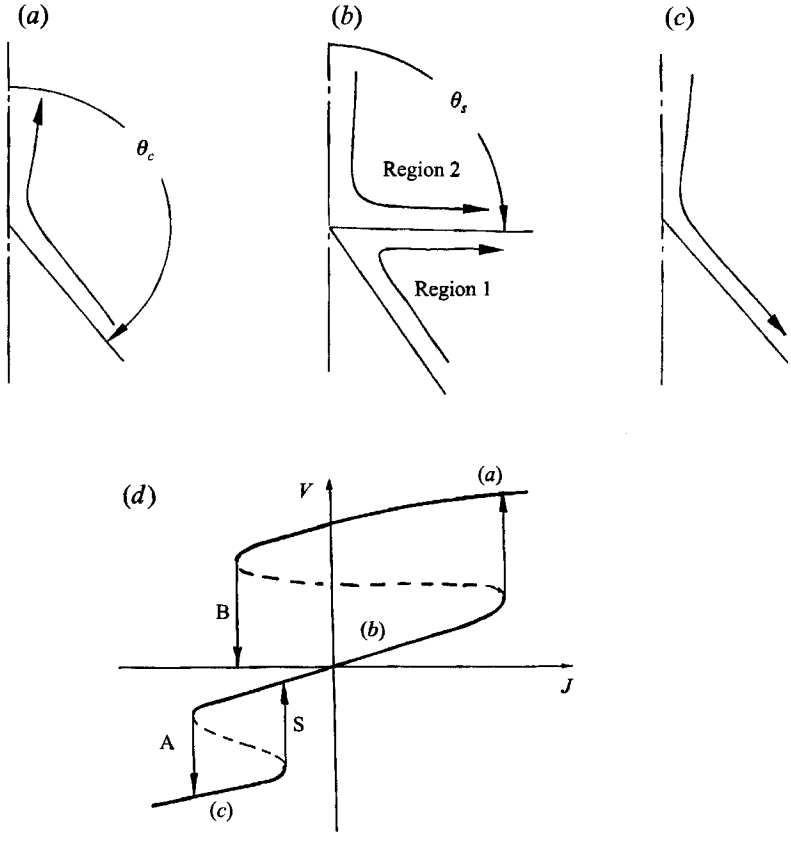

FIGURE 3. Typical patterns (*a–c*) of the meridional flow, and schematic (*d*) of hysteretic transitions between regimes with patterns (*a–c*) related to vortex breakdown (B), consolidation (C), flow separation from the cone (S), and attachment (A).

vortex consolidation (C), abrupt attachment of the jet to the $\theta = \theta_c$ conical surface (A), and abrupt separation of the swirling flow from the surface (S). These jumps between steady solutions are related to some (presumably unsteady) transition processes which cannot be described by conical similarity solutions and are not considered here as we focus on steady solutions only in this paper. Inside the regions with non-unique solutions, transitions can be triggered by finite-amplitude disturbances. Numerical calculations are used to determine how the non-uniqueness and hysteresis appear as J_1 and Γ_c increase. To understand the nature of the jumps in swirling jets for high J_1 and Γ_c, an asymptotic analysis scheme is developed. This analysis consists of finding analytical solutions of the Euler equations, and analytical or numerical solutions of the boundary layer equations. Note that the boundary layer scales and equations are different among the flow patterns (*a–c*) shown in figure 3. Therefore, the jumps between the regimes cannot be found using only one specified boundary layer problem. One needs to start from the full NSE and then consider the boundary layer limits for each viscous layer of each flow pattern in figure 3(*a–c*).

Thus, the aim of this paper is (i) to reveal the nature of the jump transitions in swirling jets, (ii) to overcome the limitations of Long's approach and to generalize it, (iii) to develop an asymptotic analysis of the conically similar swirling jets, (iv) to model outer flows in vortex devices, and (v) to present new paradoxical features of the swirling flows and to explain them.

2. Problem formulation

2.1. *Reduction of Navier–Stokes equations to ordinary differential equations*

We consider steady flows of a viscous incompressible fluid possessing conical similarity with the representation

$$\left.\begin{aligned} &v_r = -\nu\psi'(x)/r; \quad v_\theta = -\nu\psi(x)/(r\sin\theta); \quad v_\phi = \nu\Gamma(x)/(r\sin\theta);\\ &p = p_\infty + \rho\nu^2 q(x)/r^2; \quad \Psi = \nu r\psi(x); \quad x = \cos\theta. \end{aligned}\right\} \tag{1}$$

Here (r, θ, ϕ) are the spherical coordinates; r is the distance from the origin; θ and ϕ are polar and azimuthal angles (figure 2); v_r, v_θ, v_ϕ, and Ψ are velocity components and the Stokes stream function; ψ, q and Γ are dimensionless functions (Γ is a circulation along the circle, $r\sin\theta = \text{const}$, divided by $2\pi\nu$); and the prime denotes differentiation with respect to x.

Substitution of (1) into the Navier–Stokes equations, exclusion of pressure, and simple calculations yield and ODE system:

$$(1-x^2)\psi' + 2x\psi - \tfrac{1}{2}\psi^2 = F, \quad (1-x^2)F'' + 2xF' - 2F = \Gamma^2, \quad (1-x^2)\Gamma'' = \psi\Gamma'. \tag{2a–c}$$

The derivation of (2) has an interesting history. Slezkin (1934) found for $\Gamma \equiv 0$ that the NSE are reduced to (2*a*) with F being a quadratic polynomial of x. This was then independently rediscovered by Landau (1944) and Squire (1952) for the construction of their analytical solutions. For swirling flows Goldshtik (1960) found that the use of an auxiliary function F defined by

$$(1-x^2)F''' = 2\Gamma\Gamma' \tag{3}$$

drastically eases the analysis. Goldshtik (1960) and Serrin (1972) used (2*a*), (2*c*) and (3) to prove the theorems for existence and non-existence of solutions in their problems. The use of F also eases the asymptotic analysis discussed below. Equation (3) was integrated in Sozou (1992), and it leads to (2*b*) when there is no singularity on the axis, $x = 1$.

2.2. *Boundary conditions*

Since the axis in our problem is free from flow sources, except at the origin, velocity must be bounded at $x = 1$. Then it follows from (1) that

$$\psi(1) = 0, \quad \Gamma(1) = 0. \tag{4a, b}$$

However, conditions (4) do not exclude the possibility of a logarithmic singularity in radial velocity (Serrin 1972). For the dimensionless radial velocity,

$$u = rv_r/\nu = -\psi',$$

to be bounded, one needs to add to (4) the requirement $|\psi'(1)| < \infty$. This requirement yields that an integration constant is zero at the transformation (3) into (2*b*). Condition (4*a*), equation (2*a*) and its derivative yield conditions for F:

$$F(1) = 0, \quad F'(1) = 0. \tag{5a, b}$$

In our numerical calculations, we use a shooting method and integrate (2) from $x = 1$ to $x = x_c$. To start the integration, in addition to the initial conditions (4) and (5) we need some tentative values of $\Gamma'(1)$, $\psi'(1)$, and $F''(1)$. The latter two cannot be found from (2*a*) and (2*b*) owing to indeterminacies of '0/0' type at $x = 1$. However, the similar indeterminacy in (2*c*) can be resolved to obtain $\Gamma''(1) = -\frac{1}{2}\psi'(1)\Gamma'(1)$. Tentative values must be chosen to satisfy the boundary conditions at the surface, $x = x_c$,

$$\psi(x_c) = 0, \quad \Gamma(x_c) = \Gamma_c, \tag{6a, b}$$

which represent the impermeability of the cone boundary where circulation $\Gamma_c = K/\nu$ is given. As the problem is symmetric with respect to clockwise and counterclockwise swirls, and the meridional motion does not depend on the sign of Γ_c, we will use $\Gamma_c \geqslant 0$ hereafter. Besides (6), an additional (integral) relation to find the tentative values is that the flow force is given.

2.3. *The flow force*

The axial flow force acting at a spherical section, $r = \text{const}$ and $0 \leqslant \theta \leqslant \theta_c$, is

$$J = 2\pi r^2 \int_{x_c}^{1} \Pi_{rz}\,\mathrm{d}x,$$

where

$$\Pi_{rz} = \Pi_{rr}\cos\theta - \Pi_{r\theta}\sin\theta,$$
$$\Pi_{rr} = \rho v_r^2 + p - 2\rho\nu\,\partial v_r/\partial r = (\rho\nu^2/r^2)(u^2+q+2u),$$
$$\Pi_{r\theta} = \rho v_r v_\theta - \rho\nu[r^{-1}\,\partial v_r/\partial\theta + r\partial(v_\theta/r)/\partial r] = [\rho\nu^2/(r^2\sin\theta)]\,[(1-x^2)\,u' - 2\psi - u\psi],$$

so that

$$\left.\begin{aligned} J &= 2\pi\rho\nu^2 J_1, \quad J_1 = \int_{x_c}^{1} j\,\mathrm{d}x, \\ j &= x[u(u+2)+q] + \psi(u+2) - (1-x^2)\,u', \end{aligned}\right\} \tag{7}$$

where the dimensionles flow force J_1 and its density j are introduced.

Pressure can be calculated with the help of the relation (Goldshtik 1981)

$$q = xu' - \psi(\psi + xu)/(1-x^2) = (2x\psi - xF' - \psi^2)/(1-x^2). \tag{8}$$

Equation (8) is used to exclude pressure from (7) and rewrite the relation for j in the form $j = j_n + j_l$ where

$$j_n = xu^2 - \psi(u + x\psi)/(1-x\xi^2) - (\psi^2)' \tag{9}$$

and

$$j_l = (F + x^2 u + \psi^2/2)' = [(1-2x^2)\,\psi' + 2x\psi]'. \tag{10}$$

Therefore, the flow force can be represented as a sum $J_1 = J_{1n} + J_{1l}$ where

$$J_{1l} = \int j_l\,\mathrm{d}x = u(1) + (1-2x_c^2)\,u(x_c) \quad \text{and} \quad J_{1n} = \int j_n\,\mathrm{d}x. \tag{11}$$

Thus, J_{1l} depends linearly on the boundary velocities while J_{1n} is nonlinear contribution of the velocity field to the flow force. To compute J_1, we integrate (2) together with

$$J'_{1x} = x\{(2-\psi')\,\psi' - [\psi(2x-\psi) - xF']/(1-x^2)\} - F', \quad J_{1x} = \int_x^1 j\,\mathrm{d}x, \tag{12}$$

so that $J_1 = J_{1x}(x_c)$. Since at $x = 1$, J'_{1x} is undetermined, we use the Taylor expansion of ψ and F in (12) to obtain $J'_{1x}(1) = \frac{1}{2}F''(1) - \psi'(1)(\psi'(1)-3)$.

After integration, $J_{1x}(x_c)$, $\psi(x_c)$ and $\Gamma(x_c)$ must match prescribed values. Starting from initial guesses of $\psi'(1)$, $\Gamma'(1)$, and $F''(1)$, we adjust these parameter values using the Newton shooting algorithm. For very small Γ_c and J_1 the shooting iterations converge because the problem nonlinearity is weak. Once converged solutions for given Γ_c and J_1 are obtained, we increase Γ_c and J_1 gradually using the previous values of $\psi'(1)$, $\Gamma'(1)$, and $F''(1)$ as the initial data for the shooting. The numerical calculations are also consistent with the asymptotic analysis when either Γ_c or J_1, or both tend to infinity.

3. Asymptotic analysis

3.1. *Reduced Euler equations*

The asymptotic analysis helps us to understand the nature of jumps, the structure of the swirling flows, and the contributions of different flow regions to the flow force. Our technique encompasses further development and generalization of those used by Paull & Pillow (1985), Foster & Smith (1989) and SH. From the physical point of view, the parameters Γ_c and $|J_1|^{1/2}$ can be considered as the Reynolds numbers characterizing the swirl and the meridional motion respectively. We expect the usual result: at high Reynolds numbers, there are wide regions of the flow field where viscous effects are negligible, and there are thin boundary and inner layers where viscosity cannot be ignored.

In the inviscid regions one can use the Euler equations which for the conical similarity class reduce to an ODE system similar to (2) but with the linear terms in the left-hand sides of (2*a*) and (2*c*) omitted:

$$\psi^2 = -2F, \quad (1-x^2)F'' + 2xF' - 2F = \Gamma^2, \quad \psi\Gamma' = 0. \tag{13a–c}$$

We expect that the viscous layers correspond to jumps or other singularities of flow quantities in solutions of (13). The arrangement of the viscous layers and inviscid regions depend on Γ_c and J_1. We will show the solution non-uniqueness and folds for each of the flow patterns in figures 3(*a–c*). It is more instructive to start from the two-cell flow pattern (figure 3*b*).

3.2. *Two-cell flow*

3.2.1. *Inviscid regions*

It follows from (13*c*) that $\Gamma' \equiv 0$ except at points where $\psi = 0$, i.e. $\Gamma(x)$ is a step function. Note that $\Gamma \equiv$ const satisfies not only (13*c*) but also (2*c*). Owing to the different boundary conditions, $\Gamma(x_c) = \Gamma_c \neq 0$ and $\Gamma(1) = 0$, function $\Gamma(x)$ must jump at some x. In the two-cell regime, the jump occurs exactly at the separating cone, $x = x_s$ (at $\theta = \theta_s$ in figure 3*b*). Physically, inside the near-surface cell in figure 3(*b*), the angular momentum is transported to $x = x_s$ from $x = x_c$ where Γ is not zero. However, in the near-axis cell, the flow is toward $x = x_s$ from the axis where the circulation is zero (see figure 4*a*). Thus, the solution of (13*c*) is

$$\Gamma = \Gamma_1 \equiv \Gamma_c \quad \text{in} \quad x_c \leqslant x < x_s \quad \text{(region 1)}, \tag{14a}$$

and

$$\Gamma = \Gamma_2 \equiv 0 \quad \text{in} \quad x_s < x \leqslant 1 \quad \text{(region 2)}, \tag{14b}$$

where subscripts 1 and 2 relate to regions 1 and 2 respectively. Then it follows from (3) and (14) that $F_1''' \equiv 0$ and $F_2''' \equiv 0$. However, (13*b*) and (14) indicate that F'' has a jump at $x = x_s$. Therefore, F is a quadratic polynomial although it is different in regions 1 and 2. Applying the matching conditions at $x = x_s$: $F_1 = F_2, F_1' = F_2', F_1'' - F_2'' = \Gamma_c^2/(1-x_s^2)$, the condition $F_1(x_c) = 0$ from (6) and (13*a*), and (5) we have

$$F_1 = -\Gamma_c^2(x-x_c)\,[2x_s-(1+x_s)\,x_c-(1+x_s-2x_c)\,x]/[2(1+x_s)(1-x_c)^2] \tag{15a}$$

and

$$F_2 = -\Gamma_c^2(1-x)^2(x_s-x_c)^2/[2(1-x_s^2)(1-x_c)^2], \tag{15b}$$

Finally, the inviscid solutions for the stream function follow from (13*a*),

$$\psi_1 = \psi_s\{(x-x_c)\,[2x_s-(1+x_s)\,x_c-(1+x_s-2x_c)\,x]/(1-x_s)\}^{1/2}/(x_s-x_c), \tag{16a}$$

$$\psi_2 = -\psi_s(1-x)/(1-x_s), \tag{16b}$$

where

$$\psi_s = \Gamma_c(x_s-x_c)(1-x_s)^{1/2}/[(1-x_c)(1+x_s)^{1/2}]. \tag{16c}$$

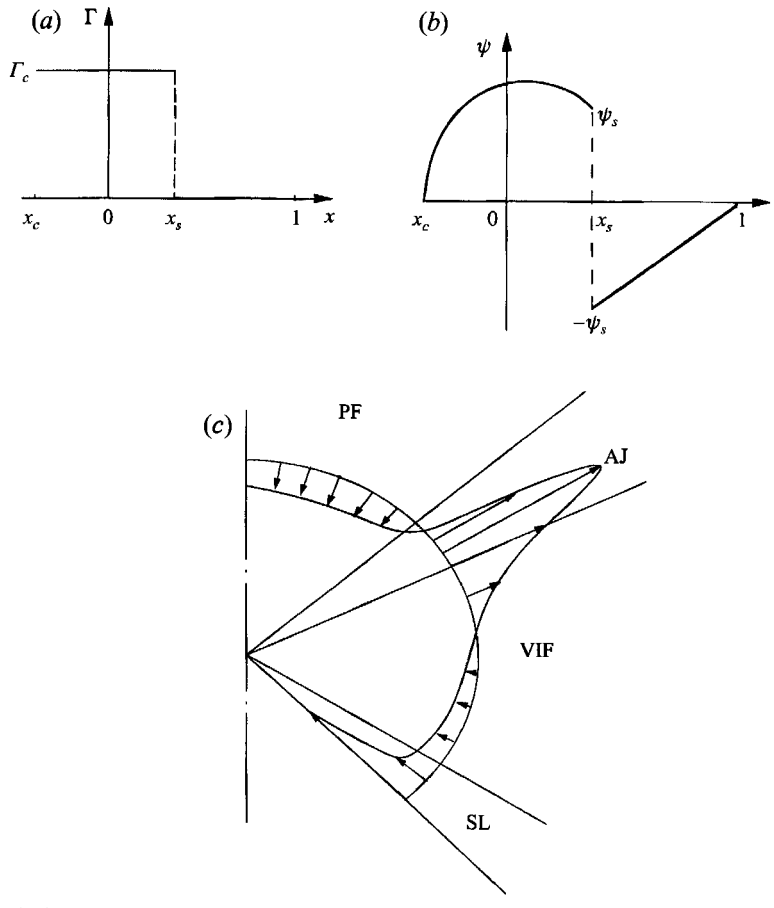

FIGURE 4. Inviscid solutions for (*a*) circulation Γ and (*b*) stream function ψ; (*c*) structure of a two-cell flow (see figure 3*b* also) with regions of potential flow PF and vortical inviscid flow VIF, a viscous annular jet AJ, and a near-surface layer SL.

The different signs of ψ_1 and ψ_2 are due to the different flow directions in the cells (figure 3*b*), and as a result, there is the jump in the stream function from $\psi_1(x_s-0) = \psi_s$ to $\psi_2(x_s+0) = -\psi_s$ (figure 4*b*). For the radial velocity we have $u_1(x_s-0) = -u_2(x_s+0) = \psi_s/(1-x_s)$. This means that inviscid flows collide, having the same absolute values but opposite signs both for v_r and v_θ at the separating surface, $x = x_s$. Swirl velocity v_ϕ jumps to zero at $x = x_s$, and the inviscid flow is swirl-free in region 2.

As the vorticity components for conical flows are

$$\omega_r = -\nu r^{-2}\Gamma', \quad \omega_\theta = 0, \quad \omega_\phi = -\nu r^{-2}\psi'',$$

we see that ω_r is zero in both regions, while ω_ϕ is zero in region 2 but not in region 1. Therefore, we have potential flow in region 2 and vortical inviscid flow in region 1. The question now arises: what is the physical reason for the vortical flow in region 1? Vorticity is advected by inviscid flow; since streamlines come from infinity where vorticity is zero, vorticity must be zero in the whole region. This reasoning is indeed valid for region 2. However, in region 1, streamlines come from the near-surface boundary layer and go to the viscous annular jet: figure 4(*c*) shows a schematic of the inviscid regions and viscous layers for the two-cell pattern. These two viscous layers, the annular jet and near-surface boundary layer, provide the main contributions to

the flow force in comparision to potential flow and vortical inviscid flow, and play a crucial role in our explanation of multi-stability (§§3.2.5 and 3.3.2). In the two-cell regime, the most high-speed part of the flow is the viscous annular jet.

3.2.2. *Annular jet*

Viscosity smooths the jumps in Γ and ψ shown in figure 4. Near $x = x_s$, the radial velocity, $u = -\psi'$, has large positive values, i.e. there is a strong outflow. Fluid, coming from regions 1 and 2 (figure 3*b*), forms an annular jet fanning out along the separating conical surface. To find a solution for ψ inside this inner viscous layer, we need to consider (2*a*) and a 'blown up' view of the vicinity of $x = x_s$ by introducing an inner variable $\xi = A(x-x_s)$, where A is expected to be $O(\psi_s)$. As F, defined by (15), is continuous at $x = x_s$, we can replace F by $F(x_s) = -\frac{1}{2}\psi_s^2$ inside the annular jet:

$$(1-x^2)\,\psi' + 2x\psi - \tfrac{1}{2}\psi^2 = -\tfrac{1}{2}\psi_s^2. \tag{17}$$

By substituting $x = x_s + \xi/A$ and $\psi = -\psi_s V_1(\xi)$, taking into account that $\mathrm{d}/\mathrm{d}x = A\,\mathrm{d}/\mathrm{d}\xi$, dividing all terms by $-\frac{1}{2}\psi_s^2$, specifying $A = \psi_s/[2(1-x_s^2)]$, and allowing $\psi_s \to \infty$, we obtain $\mathrm{d}V_1/\mathrm{d}\xi = 1 - V_1^2$, and thus $V_1 = \tanh\xi$. Therefore,

$$\psi = -\psi_s \tanh\xi \quad \text{where} \quad \xi = (x-x_s)\,\psi_s/[2(1-x_s^2)]. \tag{18}$$

This solution corresponds to a conical annular jet with a radial velocity profile,

$$u/u_s = U_2(\xi), \quad U_2 = \cosh^{-2}\xi, \quad u_s = \tfrac{1}{2}\Gamma_c^2(x_s-x_c)^2[(1+x_s)(1-x_c)]^{-2}, \tag{19}$$

which coincides with the one for the Schlichting plane jet (Schlichting 1979). However, note that the dependence of the maximal velocity and jet thickness on r is different for the conical and Schlichting jets, as these jets are physically different.

Stream function (18) for the inner viscous solution is matched as $\xi \to \pm\infty$ with the outer inviscid solutions (16*a*, *b*) at $x = x_s \pm 0$. According to (19), $u \sim O(\Gamma_c^2)$ within the jet and tends to zero as $\xi \to +\infty$. However, outside the jet the radial velocity is not zero but is only $O(\Gamma_c)$. Therefore, to match the radial velocities one needs to consider the next term in the asymptotic expansion,

$$\psi = -\psi_s V_1(\xi) + V_0(\xi), \quad u = u_s U_2(\xi) - \psi_s U_1(\xi). \tag{20}$$

Then calculations yield

$$V_0 = 2(1+x_s)\,\xi\tanh\xi - (1-x_s)(\tanh^2\xi - \xi^2\cosh^{-2}\xi), \tag{21a}$$

$$U_1 = \tanh\xi + \xi\cosh^{-2}\xi)/(1-x_s) - [(1+\xi^2)\tanh\xi - \xi]\,(1+x_s)^{-1}\cosh^{-2}\xi. \tag{21b}$$

One can see from (20), (21) and (16) that the radial velocity is matched at $x = x_s \pm 0$. Also, it follows from (18)–(21) that the position, $x = x_{max}$, of the maximal radial velocity is shifted slightly from the separating surface, $x = x_s$, toward the vortical inviscid flow: $x_{max} = x_s - 4(1+x_s)^3(1-x_s^2)(x_s-x_c)^{-2}\Gamma_c^{-2}$.

3.2.3. *Near-surface layer*

When $x \to x_c$ in solution (16*a*) for the vortical inviscid flow, the stream function goes to zero but the radial velocity tends to infinity. To avoid this singularity, one has to include viscosity in the vicinity of the surface. We expand this vicinity with the help of the scaling

$$\eta = \alpha(x-x_c), \tag{22}$$

and to make the convective and viscous terms of the same order of magnitude we use

$$\psi = \alpha(1-x_c^2)\,W(\eta) \quad \text{and} \quad \alpha = [\Gamma_c^2(x_s-x_c)(1+x_c)(1+x_s)]^{1/3}/(1-x_c^2). \tag{23}$$

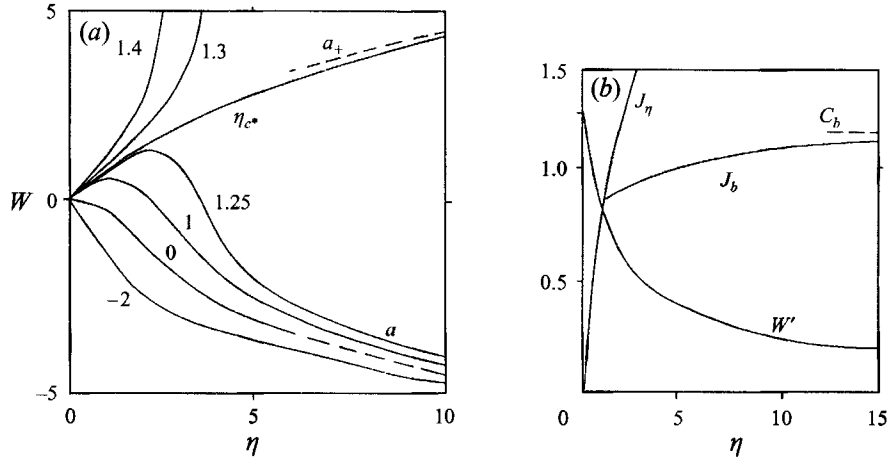

FIGURE 5. (*a*) Matching of solutions for the near-surface layer and vortical inviscid flow (figure 4*c*). Solid curves show normalized stream function W versus inner coordinate η. Numbers are values of $dW/d\eta$ at $\eta = 0$. Dashed curves show attracting (a_-) and repelling (a_+) asymptotes. The curve corresponding to $\eta_{c*} = 1.2836$ matches outer solution a_+. (*b*) Distributions of radial velocity W' and flow force J_η in the surface layer. C_b is the asymptote of $J_b = J_\eta - \frac{1}{2}\ln\eta$ as $\eta \to \infty$.

Inside the boundary layer, we apply

$$F = F_1 + d, \quad d = (1-x_c^2)\,\psi'(x_c), \tag{24}$$

to correct F_1 (see (15*a*)) near $x = x_c$. We expect that d is of a smaller order of magnitude than F_1 as $\Gamma_c \to \infty$, and therefore one can neglect d where $F_1 \neq 0$. However, one needs to take d into account near $x = x_c$ because $F_1(x_c) = 0$.

Using (22)–(24) in (2*a*) and allowing $\alpha \to \infty$ yields

$$dW/d\eta = \tfrac{1}{2}W^2 - \eta + \eta_c, \quad \eta_c = \psi'(x_c)/[\alpha^2(1-x_c^2)]. \tag{25}$$

We expect η_c to be a finite non-zero number yet to be determined. Equation (25) is integrated numerically from $\eta = 0$ with the initial condition $W(0) = 0$. Figure 5(*a*) shows a few solutions $W(\eta)$ for different η_c (see values labelling the curves). If $\eta_c < \eta_{c*}$, then $W(\eta)$ approaches the asymptote $W = -(2\eta)^{1/2}$ (curve a_- in figure 5*a*) as $\eta \to \infty$. If $\eta_c > \eta_{c*}$, then $W(\eta)$ goes to infinity for finite $\eta = \eta_p$ as $2/(\eta_p - \eta)$. If $\eta_c = \eta_{c*}$, then $W(\eta)$ approaches the asymptote $W = (2\eta)^{1/2}$ (curve, a_+ in figure 5*a*) as $\eta \to \infty$. To match the outer solution (16*a*) one needs the value $\eta_c = \eta_{c*}$, and the shooting procedure gives $\eta_{c*} = 1.2836$.

From (23)–(25) it follows that $d = \eta_c \alpha^2 (1-x_c^2)^2$ is of $O(\Gamma_c^{4/3})$. Therefore d is indeed of a smaller order of magnitude (for large Γ_c) than F_1 which is of $O(\Gamma_c^2)$. Note that the solution of (25) for the near-surface boundary layer matches solution (16*a*) for vortical inviscid flow with respect to both the stream function and radial velocity. Here one does not need the next term of the asymptotic expansion to match u.

Finally, the asymptotic relation for the Reynolds number $Re_c = rv_{rc}/\nu$, where v_{rc} is the radial velocity on the cone surface, is

$$Re_c = -1.28\Gamma_c^{4/3}(x_s - x_c)^{2/3}[(1+x_c)(1+x_s)]^{2/3}/(1-x_c^2). \tag{26}$$

The minus sign in (26) is because the radial component of velocity is directed toward the apex at the cone surface (see figure 4*c*).

Now, having the solutions for the whole flow region, we can calculate the flow force.

3.2.4. *Decomposition of the flow force*

The flow force can be decomposed into the sum

$$J_1 = J_{PF} + J_{AJ} + J_{VIF} + J_{SL}, \tag{27}$$

where the terms on the right-hand side of (27) are contributions from the corresponding regions, defined in figure 4(*c*). Applying (16*b*) in (9) and integrating j_n from x_s to 1 we find the contribution of the potential flow (PF):

$$J_{PF} = (1-x_s)^{-2}\psi_s^2 \ln[2/(1+x_s)]. \tag{28}$$

It follows from (16*c*) that J_{PF} is of $O(\Gamma_c^2)$.

To estimate the flow force of the annular jet (AJ) we note that the main contribution is due to term xu^2 in (9) that is of $O(\Gamma_c^4)$, as follows from (19). Then $J_{AJ} \sim xu^2\delta x$, where δx is $O(\Gamma_c^{-1})$ (see (18), (16*c*)). This implies that $J_{AJ} \sim O(\Gamma_c^3)$. More detailed calculations using (18)–(21) and (9) indicate that there is no contribution of $O(\Gamma_c^2)$ to J_1 and

$$J_{AJ} = \tfrac{2}{3}x_s\psi_3^3/(1-x_s^2) + O(\Gamma_c). \tag{29}$$

To find the contribution from the vortical inviscid flow, J_{VIF}, we substitute (16*a*) in (9) and decompose j_n in two parts: $j_n = j_{nr} + j_{ns}$, where j_{nr} is a 'regular' part that gives $J_{Vr} \sim O(\Gamma_c^2)$. The analytical expression for J_{Vr} is rather lengthy; since this term is not crucial for the total flow force, we omit it. The singular part is

$$j_{ns} = c/(x-x_c), \quad c = \tfrac{1}{2}\Gamma_c^2 x_c(x_s-x_c)/[(1-x_c)(1+x_s)]. \tag{30}$$

If one tries to integrate (30) from x_c to x_s, the integral diverges owing to the pole of j_{ns} at $x = x_c$. To overcome this difficulty we integrate (30) from $x_m = x_c + \alpha^{-1/2}$ to x_s, where α is defined by (23), which gives

$$J_{Vs} = c[\ln(x_s-x_c) + \tfrac{1}{2}\ln\alpha]. \tag{31}$$

To find a contribution from interval (x_c, x_m) to the flow force we use the near-surface boundary-layer solution (SL). Substituting the inner variables (22) and (23) in (9) we find that, to the leading order,

$$j_n = x_c(1-x_c^2)^2\alpha^4(\mathrm{d}W/\mathrm{d}\eta)^2. \tag{32}$$

As $\eta \to \infty$, $(\mathrm{d}W/\mathrm{d}\eta)^2 \to 1/(2\eta)$ because $W \to (2\eta)^{1/2}$. Therefore if one integrates (32) from $\eta = 0$ to $\eta = \infty$, the integral diverges logarithmically. However to cover interval (x_c, x_m) we need to integrate (32) only up to $\eta_m = \alpha^{1/2}$, which gives

$$J_L = x_c(1-x_c^2)^2\alpha^3(C_b + \tfrac{1}{4}\ln\alpha), \quad C_b = 1.21). \tag{33}$$

To find C_b, (32) is integrated together with (25). Figure 5(*b*) shows the calculated distributions of

$$W' = \mathrm{d}W/\mathrm{d}\eta, \quad J_\eta = \int_0^\eta (\mathrm{d}W/\mathrm{d}\eta_1)^2\,\mathrm{d}\eta_1 \quad \text{and} \quad J_b = J_\eta - \tfrac{1}{2}\ln\eta$$

(J_b is defined in the range $1 \leqslant \eta < \infty$). In contrast to J_η, J_b is bounded; figure 5(*b*) shows how J_b approaches its limit C_b as $\eta \to \infty$. Combining (31) and (33) and substituting α from (23) we find that the contribution of the near-surface layer to J_1 is

$$J_{SL} = x_c(x_s-x_c)[3(1-x_c)(1+x_s)]^{-1}\Gamma_c^2\ln\Gamma_c + O(\Gamma_c^2). \tag{34}$$

At $x_c = -1$, (34) is reduced to $J_{SL} = (-1/6)\Gamma_c^2\ln\Gamma_c$ which coincides with the result of Paull & Pillow (1985) for a flow induced by a half-line vortex.

Thus we see for the terms in (27) that $J_{AJ} \sim O(\Gamma_c^3)$, $J_{SL} \sim O(\Gamma_c^2\ln\Gamma_c)$, and the contribution from the inviscid regions is of $O(\Gamma_c^2)$, i.e. the annular jet provides the main

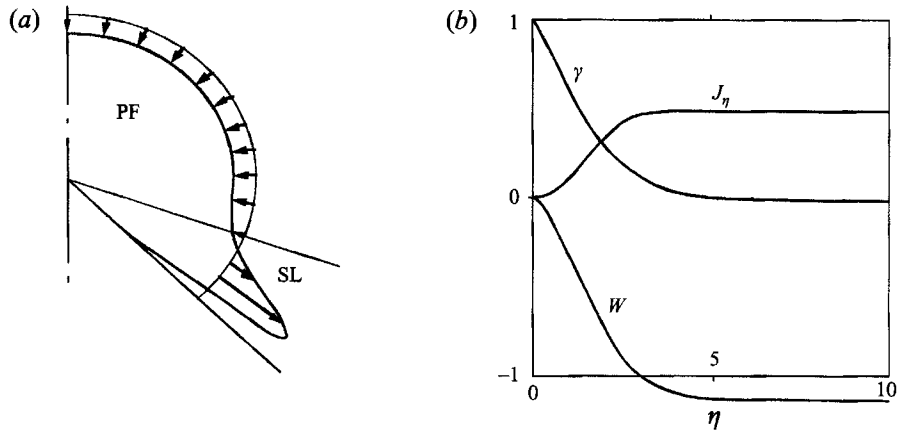

FIGURE 6. (*a*) One-cell flow with potential flow PF and near-surface boundary layer SL. (*b*) Distributions of stream function W, circulation γ, and flow force J_η in the SL shown in (*a*).

contribution to the flow force as $\Gamma_c \to \infty$. Therefore, to calculate the flow force of the two-cell flow at high Γ_c, we need to take into account only J_{AJ}. This is enough to reveal non-uniqueness of solutions.

3.2.5. *Non-uniqueness of two-cell regimes*

Using (16*c*) in (29) we obtain at leading order

$$J_1 = \tfrac{2}{3}\Gamma_c^3 x_s(x_s - x_c)^3(1-x_s)^{1/2}(1+x_s)^{-5/2}(1-x_c)^{-3}. \tag{35}$$

It follows from (35) that for any fixed Γ_c and x_c, J_1 is a non-monotonic function of x_s with zeros at $x_s = 0$, $x_s = 1$ and $x_s = x_c$. (It will be shown below that this means that J_1 has a smaller order of magnitude than Γ_c^3). For $0 < x_s < 1, J_1 > 0$ and, therefore, there is a maximum of $J_1 (= J_{1max})$ inside the interval $x_c < x_s < 1$. This implies that for each value of J_1 in the range $0 < J_1 < J_{1max}$, there are at least two values of x_s, i.e. two different two-cell regimes!

If $x_c < 0$, then $J_1 < 0$ for $x_c < x_s < 0$. Since $J_1 = 0$ at $x_s = 0$ and $x_s = x_c$, there is also a minimum of $J_1 (= J_{1min})$ inside the interval $x_c < x_s < 0$. This means that for each value of J_1 in the range $J_{1min} < J_1 < 0$, there are at least two values of x_s. So there are two different two-cell regimes for both positive and negative values of J_1. Each extremum of J_1 means that surface $V = f(J_1, \Gamma_c)$ – where V is any parameter resulting from the solution – has a fold (similar to those in figure 3(*d*) that can be interpreted as a section of $V(J_1, \Gamma_c)$, e.g. when $\Gamma_c = \text{const}$). It follows from the above analysis that there are two folds when $x_c < 0$ and one fold when $x_c \geqslant 0$. The fold corresponding to J_{1max} relates to a jump like C in figure 3(*d*), and the fold corresponding to J_{1min} relates to a jump like A in figure 3(*d*).

Thus, the asymptotic analysis reveals solution non-uniqueness for large Γ_c and J_1. We have found that there are at least two solutions. To show that the number of solutions and number of folds are more than two, we have to consider regimes with a one-cell inviscid region. We start with the simpler case when the flow in the inviscid region is potential.

3.3. *Regime with near-surface outflow*

The results of §3.2 do not cover the cases when $x_s = x_c$ or $x_s \to x_c$ as $\Gamma_c \to \infty$ because (16*a*) would then yield $\psi_s = 0$. Therefore, the regime, schematically shown in figure 6(*a*), must be studied separately. In contrast to the two-cell case (figure 4*c*), now there

is no vortical inviscid flow region in figure 6(*a*). However, potential flow and near-surface boundary layers occur in both the cases.

3.3.1. *Potential flow*

The solution for potential flow is similar to that in §3.2.1:

$$\Gamma \equiv 0, \quad \psi_2 = -\psi_s(1-x)/(1-x_c) \quad \text{in} \quad x_c < x \leqslant 1, \tag{36}$$

and

$$J_{PF} = \psi_s^2(1-x_c)^{-2}\ln[2/(1+x_c)]; \tag{37}$$

however, here parameter ψ_s is not defined by (16*c*) but must be found from matching conditions for the potential flow and near-surface boundary layer.

3.3.2. *Near-surface jet*

The shear-layer problem for the near-surface jet is different from that in §3.2.3. because now Γ is not constant across the surface layer but varies from Γ_c at $x = x_c$ to zero at the outer boundary of the surface layer as follows from (36). This produces different inner scales and boundary-layer equations. Introducing the inner variables

$$\left.\begin{aligned} &\psi = \alpha(1-x_c^2)\,W(\eta), \quad F = \alpha^2(1-x_c^2)^2\,\Phi(\eta), \quad \Gamma = \Gamma_c\,\gamma(\eta), \\ &\eta = \alpha(x-x_c), \quad \alpha = \Gamma_c^{1/2}(1-x_c^2)^{-3/4}, \end{aligned}\right\} \tag{38}$$

substituting them in (2), and allowing $\Gamma_c \to \infty$, we get

$$W' = W^2/2 + \Phi, \quad \gamma'' = W\gamma', \quad \Phi'' = \gamma^2. \tag{39}$$

Here the prime denotes differentiation with respect to η. The boundary conditions at the surface are transformed from (6) to $W(0) = 0$ and $\gamma(0) = 1$. To match with (36), one needs to satisfy the conditions, $\gamma \to 0$ and $\Phi' \to 0$ as $\eta \to \infty$. For this, $\gamma'(0)$ and $\Phi'(0)$ must be found (e.g. by the shooting procedure). $W'(0) = \Phi(0)$ is a free parameter, which is related to $Re_c = rv_r(x_c)/\nu = -\Gamma_c(1-x_c^2)^{-1/2}\Phi(0)$.

To find a contribution from the near-surface layer to the flow force we use (32) and substitute α from (38), which yields

$$j_n = x_c\,\Gamma_c^2(1-x_c^2)^{-1}\,W'^2, \tag{40}$$

and after integration of (40) we have

$$J_{SL} = x_c\,\Gamma_c^{3/2}(1-x_c^2)^{-1/4}\,J_\infty, \quad J_\infty = \int_0^\infty W'^2\,\mathrm{d}\eta. \tag{41}$$

One more matching condition is that the value of the stream function from the inviscid solution (36) at $x = x_c$ must coincide with that from the boundary-layer solution of (39) at $\eta = \infty$, which gives

$$\psi_s = -\Gamma_c^{1/2}(1-x_c^2)^{1/4}\,W(\infty). \tag{42}$$

Substitution of (42) in (37) yields that

$$J_{PF} = \Gamma_c(1-x_c^2)^{-3/2}\,W^2(\infty)\ln[2/(1+x_c)].$$

Therefore, J_{PF} is of $O(\Gamma_c)$ while, as follows from (41), J_{SL} is of $O(\Gamma_c^{3/2})$ (except in the case $x_c = 0$ studied in SH where J_{SL} is of $O(\Gamma_c)$).

Since the potential flow is directed to the cone (figure 3*c*), ψ is negative and $\psi_s > 0$ from (36). It follows from (42) that $W(\infty)$ must be negative. Let us conjecture that $W(\infty)$ is a non-zero finite number. Then one can see from (39) that γ and Φ' decay

$W'(0)$	$-W''(0)$	$-\gamma'(0)$	J	$-W(\infty)$	η_{sep}	Comments
−64	0.0683	5.66	40.1	11.3	0	Transition to the SL with
−40	0.0864	4.47	23.6	8.95	0	weak swirl
−20	0.122	3.16	11.8	6.32	0	—
−10	0.173	2.24	5.93	4.48	0	—
−3.5	0.290	1.33	2.12	2.67	0	—
−1	0.508	0.754	1.27	2.06	0	—
−0.116	0.789	0.469	0.498	1.13	0	Minimal flow force J
0	0.848	0.43	0.507	1.09	0	Flow separation
1	1.56	0.159	1.94	1.17	2.17	—
2.5	3.25	0.027	36.3	2.45	3.69	Transition to two-cell regime

TABLE 1. Characteristics of the near-surface layer (SL)

exponentially as $\eta \to \infty$. Then W' also decays exponentially and thus W and Φ tend exponentially to negative constant values. Therefore, the above conjecture is correct. Since W' decays exponentially, the integral in (41) converges.

The flow pattern inside the near-surface layer can be one-cellular or two-cellular depending on $\Phi(0)$. Table 1 shows the dependence of the main characteristics of the near-surface boundary layer on $\Phi(0)(= W'(0))$. In particular, one can see that J_∞ has the minimum value $J_\infty = J_{\infty\, min} = 0.4984$ at $\Phi(0) = -0.116$, i.e.

$$J_{SL,ext} = 0.4984 x_c \Gamma_c^{3/2}(1-x_c^2)^{-1/4}. \tag{43}$$

Subscript *ext* means an 'extremum' that is a minimum for $x_c \geqslant 0$ and a maximum for $x_c < 0$. The minimum is reached in the one-cell flow. Figure 6(*b*) shows distributions of stream function W, swirl γ, and the flow force J_η at $J_\infty = J_{\infty\, min}$. For positive $W'(0)$, when the near-surface boundary layer becomes two-cellular, the value η_{sep} (where $W = 0$) is shown in the last column. There is the tendency for $J_\infty \to \infty$ as $\eta_{sep} \to \infty$, which means transition from (41) to (34).

Since there is also the tendency for $J_\infty \to \infty$ as $W'(0) \to -\infty$ (table 1), this means that (41) changes in this limiting case as well. To find the new asymptotic relation, we note that the meridional motion dominates the swirl as $W'(0) \to -\infty$. Therefore, we can neglect the swirl when considering the meridional motion. Then, introducing the inner variables

$$\psi = -\psi_s W(\eta), \quad \eta = \alpha(x-x_c), \quad \alpha = \tfrac{1}{2}\psi_s(1-x_c^2), \tag{44}$$

using $F = -\psi_s^2/2$, and allowing $\psi_s \to \infty$, we get from (2*a*)

$$W' = 1 - W^2, \quad W = \tanh\eta, \tag{45}$$

where the condition W(0) = 0 gives the integration constant. Applying (44) in (2*c*) and allowing $\psi_s \to \infty$ we get $\Gamma'' = -2W\Gamma'$; substituting (45) in this equation and integrating with the conditions $\Gamma(0) = \Gamma_c$ and $\Gamma(\infty) = 0$, we obtain

$$\Gamma = \Gamma_c(1-\tanh\eta). \tag{46}$$

Then matching the boundary-layer and potential solutions with respect to F' yields

$$\Gamma_c^2 = \psi_s^3/[(4\ln 2 - 2)(1-x_c)]. \tag{47}$$

Applying $Re_c = -\psi'(x_c)$, it follows from (51) and (52) that $Re_c = \psi_s^2/[2(1-x_c^2)]$, and therefore

$$\Gamma_c^4 = 2Re_c^3(1-x_c^2)(1+x_c)^2/(2\ln 2 - 1)^2. \tag{48}$$

To find a contribution of the near-surface layer in the flow force we use (44) and (45) in $j_n = x_c \psi'(x)^2$ and after integration obtain

$$J_{SL} = x_c \Gamma_c^2 (4 \ln 2 - 2)/(3 + 3x_c). \tag{49}$$

Substitution of Γ_c from (48) in (49) gives the relation

$$J_{SL} = (2^{3/2}/3)\, Re_c^{3/2}\, x_c (1 - x_c^2)^{1/2}, \tag{50}$$

which is also valid for the non-swirling near-surface jet.

Thus, there is one more extremum (i.e. fold) of J_1 in the one-cell regime with the near-surface outflow (see (43)). For the case $x_c < 0$, this fold corresponds to the maximum of J_1 and relates to transition S in figure 3(*d*). This transition occurs at a negative value of $J_1 \sim O(\Gamma_c^{3/2})$ and indicates a jump separation of the swirling flow from the surface, i.e. abrupt transition of the flow pattern from (*c*) to (*b*) in figure 3. If, after this transition, one decreases J_1 down to its negative minimum $J_{1\,min} \sim O(\Gamma_c^3)$ (see §3.2.5), then a transition of type A in figure 3(*d*) occurs. This indicates an abrupt attachment to the surface of the swirling outflow, i.e. an abrupt transition of the flow pattern from (*b*) to (*c*) in figure 3. Finally, we will show that one more fold exists for the one-cell flow with the near-axis jet (figure 3*a*).

3.4. *Outer flow of the near-axis jet*

The results of §3.2 do not cover the case when $x_s = 1$ or $x_s \to 1$ as $\Gamma_c \to \infty$ because ψ_c becomes zero in (16*c*). Therefore, this regime, whose schematic is shown in figure 7(*a*) (see also figure 3*a*), must be studied separately. In contrast to the two-cell case (figure 4*c*), now there is no potential flow region, and the viscous annular jet is transformed to a near-axis Long's jet; the near-surface boundary layer and vortical inviscid flow are common.

3.4.1. *Near-surface boundary layer*

Results for the near-surface boundary layer follow from those for the two-cell case after putting $x_s = 1$. In particular, the analysis of §3.2.3 is valid with

$$\alpha = 2^{1/3} \Gamma_c^{2/3} (1 - x_c^2)^{-2/3}, \quad Re_c = -2.03\, \Gamma_c^{4/3} (1 - x_c^2)^{-1/3}. \tag{51}$$

3.4.2. *Vortical inviscid region*

Since (16*c*) yields $\psi_s = 0$ at $x_s = 1$, the inviscid analysis must be reconsidered. Now $\Gamma \equiv \Gamma_c$ in $x_c \leqslant x < 1$, and to find the stream function distribution we first substitute (16*c*) in (16*a*), eliminate $(1 - x_s)^{1/2}$, and then put $x_s = 1$ to obtain

$$\psi_1 = \Gamma_c [(x - x_c)(1 - x)/(1 - x_c)]^{1/2}. \tag{52}$$

Substituting (52) in (9) we get after simple but lengthy calculations that

$$j_n = \tfrac{1}{4} \Gamma_c^2 [x_c (x - x_c)^{-1} - (1 + 3x_c)(1 - x_c)^{-1}(1 + x)^{-1}]. \tag{53}$$

We see that j_n has a pole at $x = x_c$ like in the case studied in §3.2.4. However, there is no pole at $x = 1$ even though ψ' has a square-root singularity at $x = 1$ according to (52). The corresponding 'pole' terms appear to cancel in the calculations.

To overcome the difficulty induced by the pole at $x = x_c$ in (52), we apply the same technique as in §3.2.4 and integrate (53) from $x_m = x_c + \alpha^{-1/2}$ to 1, where α is defined by (51), which gives

$$J_{VIF} = \tfrac{1}{4} \Gamma_c^2 \{ \tfrac{1}{2} x_c \ln \alpha + x_c \ln (1 - x_c) - (1 + 3x_c)(1 - x_c)^{-1} \ln [2/(1 + x_c)] \}. \tag{54}$$

A contribution from interval (x_c, x_m) to J_1 will be found by considering SL.

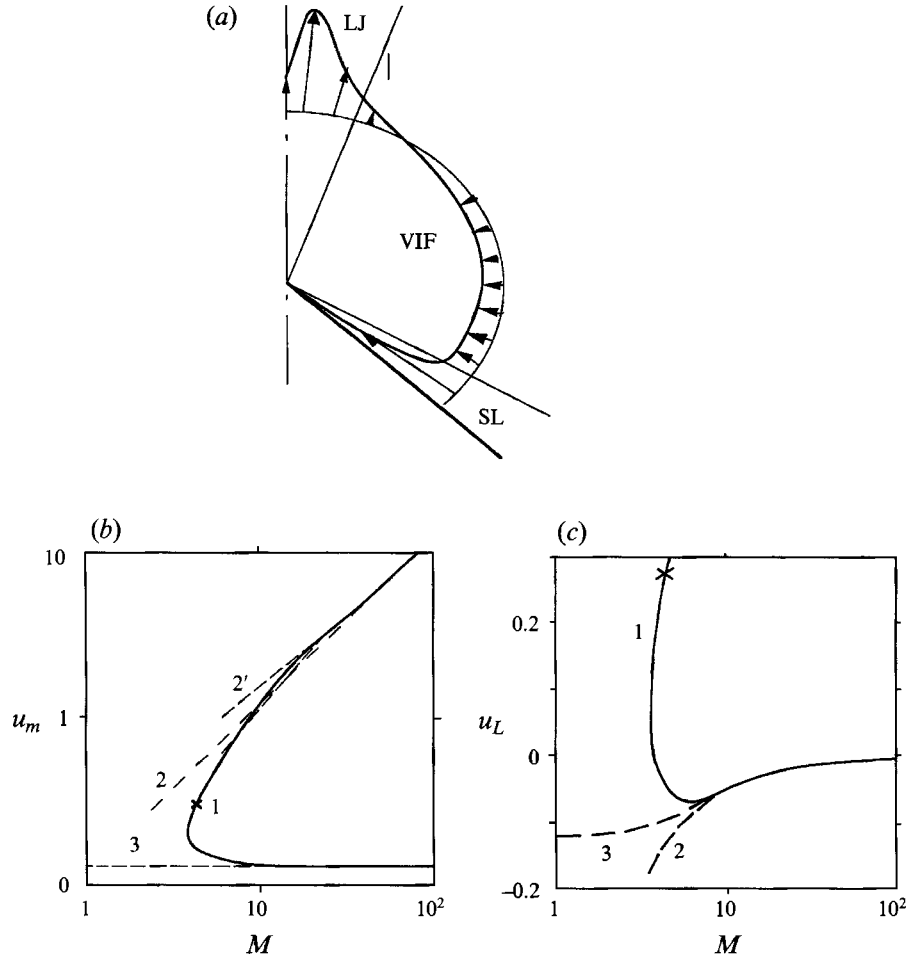

FIGURE 7. (*a*) One-cell flow with vortical inviscid flow VIF, near-surface layer SL, and Long's jet LJ. (*b*, *c*) Numerical (solid curve) and asymptotic (dashed curves) results for the dependence of the maximal radial velocity u_m (*b*) and velocity on the axis u_L (*c*) on the normalized flow force M in Long's jet.

3.4.3. *External flow force*

Reiterating the procedure used in §3.2.4 for the SL we arrive at (33) but with α now given by (51). Adding (33) to (54) and substituting α from (51) we obtain

$$\left.\begin{aligned} J_{VIF}+J_{SL} = J_{EX} &= (x_c/6)\,\Gamma_c^2 \ln \Gamma_c + \tfrac{1}{4}\Gamma_c^2 f_e(x_c), \\ f_e(x_c) &= x_c\left[2C_b + \tfrac{1}{3}\ln\frac{2(1-x_c)}{(1+x_c)^2}\right] - \frac{1+3x_c}{1-x_c}\ln\frac{2}{1+x_c}. \end{aligned}\right\} \tag{55}$$

Here J_{EX} is the contribution to J_1 from the vortical inviscid flow and near-surface boundary layers, i.e. from the whole region which is *external* with respect to the Long's jet. There are three reasons to elaborate on expression (55), where the term of $O(\Gamma_c^2)$ is not neglected in contrast with the case of the two-cell flow. The first reason is that if $x_c = 0$, then the term of $O(\Gamma_c^2 \ln \Gamma_c)$ on the right-hand side of (55) becomes zero. In this case, (55) yields $J_{EX} = -\frac{1}{4}\Gamma_c^2 \ln 2$ which coincides with the result obtained in SH for a model tornado. Secondly, as $\ln \Gamma_c$ grows very slowly as Γ_c increases, both the terms

in (55) can be used for comparison with numerical results at moderate values of Γ_c. And, finally, the third reason is that J_{LJ} (that is the contribution of Long's jet to J_1) is also of $O(\Gamma_c^2)$ (Long 1961). Therefore, one needs both the terms in (55) for detailed estimation of J_{EX} and J_{LJ}.

It follows from (55) that J_{EX} is constant for fixed Γ_c and x_c. However, J_1 is not constant owing to J_{LJ}. To compare J_{LJ} and J_{EX} we now reconsider the analysis of the near-axis flow after Long (1961), Burggraf & Foster (1977), and Foster & Smith (1989). We study in more detail two points: (i) transformation of Long's jet into the Schlichting round jet (Schlichting 1933) when swirl becomes weak in comparison with the meridional motion, and (ii) matching of Long's jet and vortical inviscid flow.

3.5. *Near-axis jet*

3.5.1. *Schlichting's jet*

We start with the case of the swirl-free round jet to deduce an improved relation for the flow force. Swirl-free conical flows are governed by Slezkin's (1934) equation that, under conditions (4) and (5), takes the form

$$(1-x^2)\psi' + 2x\psi - \tfrac{1}{2}\psi^2 = C(1-x)^2, \tag{56}$$

where $C = -Re_c(1+x_c)/(1-x_c)$. Let Re_c be bounded but $Re_a = -\psi'(1) \to \infty$. Introducing the inner variable, $\eta = Re_a(1-x)$, and considering the expansion with respect to Re_a^{-1}, we obtain

$$\psi = \psi_0 + Re_a^{-1}\psi_1 + \ldots, \quad \psi_0 = 4\eta/(4+\eta), \quad \psi_1 = -2\eta^2/(4+\eta), \tag{57}$$

where ψ_0 corresponds to Schlichting's solution.

It follows from (56) and (57) that $\mathrm{d}\psi/\mathrm{d}x \to 2$ as $\eta \to \infty$. On the other hand, the solution for the outer flow near $x = 1$ has the form, $\psi = 4 - 2(1-x) + o(1-x)$ (Goldshtik & Shtern 1990). Therefore, the inner and outer solutions are matched with respect to v_r due to the second term of expansion (57). The flow force is found by use of (57) in (9) which gives

$$J_1 = \tfrac{4}{3}Re_a - 4\ln Re_a + O(1). \tag{58}$$

Thus, the flow force of the swirl-free jet is less than that due to the main term only.

3.5.2. *Long's jet*

Using $\eta = Re_a(1-x)$ in (2) and allowing $Re_a \to \infty$ we obtain the system

$$\eta\psi' = \psi - \tfrac{1}{4}\psi^2 - \tfrac{1}{2}F, \quad \eta\gamma'' = -\tfrac{1}{2}\psi\gamma', \quad \eta F'' = F' + \tfrac{1}{2}\epsilon\gamma^2, \tag{59}$$

where the prime denotes differentiation with respect to η. Solutions of (59) must satisfy the boundary conditions on the axis,

$$\psi(0) = 0, \quad \psi'(0) = 1, \quad \gamma(0) = 0, \quad F(0) = F'(0) = 0, \tag{60}$$

and on the outer boundary of the LJ,

$$\gamma(\infty) = 1, \quad F'(\infty) = -\tfrac{1}{2}\epsilon. \tag{61}$$

Here $\epsilon^{-1} = u_L = Re_a/\Gamma_c^2$ is the rescaled velocity on the axis and $\gamma = \Gamma/\Gamma_c$. Long's problem is equivalent to (59)–(61), but formulation (59)–(61) seems to be easier for numerical calculations and analysis. In particular, one does not need the Taylor expansion for integration from $\eta = 0$ as used by Long (1961). For the integration, tentative values must be chosen for $\gamma'(0)$, $F''(0)$, and u_L. One cannot find $F''(0)$ from (59) owing to the '0/0'-type indeterminacy, but the indeterminacy solution yields

$\gamma''(0) = -\frac{1}{2}\gamma'(0)$. After integration, (61) must be satisfied, and a prescribed value of the flow force must be matched with the computed value. These three requirements yield the values of $\gamma'(0)$, $F''(0)$, and u_L with the help of the Newton shooting procedure. We use this algorithm to recalculate Long's solution over a wide range of Long's parameter $M = 2\pi J_1/\Gamma_c^2$. Solid curve 1 in figure 7(*b*) shows the calculated dependence on M of u_m where $u_m = u_s/\Gamma_c^2$ is the rescaled maximal velocity of Long's jet.

3.5.3. *Matching of Long's and Schlichting's jets*

Our goal here is to study in more detail the limiting cases as $M \to \infty$ along the upper and lower branches of curve 1 in figure 7(*b*). Above the cross on curve 1, the maximum of the radial velocity is positioned on the axis, i.e. u_m coincides with u_L. Since along the upper branch $u_L \to \infty$, we can use an expansion in ϵ:

$$\psi = \psi_0 + \epsilon\psi_1 + \ldots, \quad \gamma = \gamma_0 + \epsilon\gamma_1 + \ldots, \quad F = F_0 + \epsilon F_1 + \ldots.$$

At the zeroth order, ψ_0 is again Schlichting's solution, $F_0 \equiv 0$, and $\gamma_0 = \eta/(4+\eta)$ (Foster & Smith 1989; Goldshtik & Shtern 1990). At the first order, $F_1 = 2\ln(1+\frac{1}{4}\eta) - \frac{1}{2}\eta$, there is no analytical solution for ψ_1 but $\psi_1 = \frac{1}{8}\eta - \ln\eta + O(1)$ for $\eta \gg 1$. It yields $\mathrm{d}\psi/\mathrm{d}x = -\Gamma_c^2\,\mathrm{d}\psi_1/\mathrm{d}\eta \to -\frac{1}{8}\Gamma_c^2$ as $\eta \to \infty$. This again exactly matches the axial velocity of the outer solution for highly swirling flow (Goldshtik, Shtern & Yavorsky 1989). Straightforward calculations then give

$$J_1 = 4Re_a/3 - (\tfrac{1}{4}\Gamma_c^2 + 4)\ln Re_a. \tag{62}$$

For the case, $\Gamma_c \gg 1$, i.e. for Long's boundary layer, one can omit the 4 in the brackets. Multiplying by $2\pi/\Gamma_c^2$ and adding one more term we transform (62) to

$$M = 8\pi u_m/3 - \tfrac{1}{2}\pi \ln u_m - 2.25,$$

shown by dashed curve 2′ in figure 7(*b*). The relation $M = 8\pi u_m/3$ is also shown by line 2. Merging of the solid and dashed curves means agreement of our numerical and asymptotic results.

3.5.4. *Matching of Long's jet with the outer flow*

Along the lower branch of curve 1 in figure 7(*b*) as $M \to \infty$, Long's jet is transformed into the viscous annular jet. The value of the maximal velocity in viscous annular jet is governed by relation (19*b*) which is reduced at $x_s = 1$ to

$$u_m = \tfrac{1}{8}. \tag{63}$$

In particular, (63) means that the maximal jet velocity does not depend on x_c in the limiting case $x_s \to 1$. In figure 7(*b*), dashed line 3 showing (63) merges with curve 1 as $M \to \infty$, and therefore the maximum velocities of Long's jet and the viscous annular jet coincide.

Now, we consider matching of the axial velocity for Long's jet and the potential flow as $x_s \to 1$. Solid curve 1 in figure 7(*c*) shows the numerical results of the relation between u_L and M. In contrast to u_m, u_L varies non-monotonically along the lower branch of curve 1 (compare figures 7*b* and 7*c*). Our calculations show that the axial velocity reaches its minimum $u_{L\,min}$ ($= -0.0712$) at $M = 5.77$ and then tends to zero as M increases. The minimum of u_L is reached with a two-cell flow pattern, but the near-axis cell is thin and positioned inside Long's boundary layer. For cone $x = x_s$, separating the cells, we find $\xi_1 = 1.08$ where

$$\xi_1 = \tfrac{1}{2}\Gamma_c[(1-x_s)/(1+x_s)]^{1/2}. \tag{64}$$

For the potential flow it follows from (16*b*, *c*) that

$$Re_a = -\psi'(1) = -\Gamma_c(x_s - x_c)/[(1-x_c)(1-x_s^2)^{1/2}], \tag{65}$$

and therefore $Re_a \to -\infty$ as $x_s \to 1$. However, this just means that Re_a becomes of a higher order of magnitude with respect to Γ_c. Indeed, substituting $(1-x_s)$ from (64) in (65) and then putting $x_s = 1$ gives

$$u_L = -1/(8\xi_1). \tag{66}$$

Although (66) provides the correct order of magnitude for u_L at $\xi_1 \sim O(1)$, nevertheless again $u_L \to -\infty$ as $\xi_1 \to 0$. To overcome this drawback we use relations (18)–(21) for $x = 1$ which yields to the leading order

$$u_L = -\tanh(\xi_1)/(8\xi_1). \tag{67}$$

Since $\tanh(\xi_1)/\xi_1 \leqslant 1$, it follows that $u_L \geqslant -\frac{1}{8}$ and reaches its minimum $u_L = -\frac{1}{8}$ at $\xi_1 = 0$. Thus, the drawback of (66) is overcome in (67).

Substituting $(1-x_s)$ from (64) in (35) and then putting $x_s = 1$ gives $J_1 = \frac{4}{3}\Gamma_c^2\xi_1$ or

$$\xi_1 = \tfrac{3}{4}M/\pi, \tag{68}$$

which agrees with the corresponding result by Foster & Smith (1989). Use of (68) in (66) yields the relation, $u_L = -\pi/(6M)$, shown by dashed curve 2 in figure 7(*c*). Dashed curve 3 in figure 7(*c*) shows the result of substitution of (68) in (67).

Thus, the new results of this section are the existence of the minimal axial velocity, u_{Lmin}, and the asymptotic relations for Long's jet as $M \to \infty$ that match it with the outer flow. Besides the extrema of J_1 found for patterns (*b*) and (*c*) in figure 3, there is the minimum of J_1 for pattern (*a*); however, the Long (1961) and Burggraf & Foster (1977) results for the minimum value, $J_{1min} = M_{*L}\Gamma_c^2/(2\pi)$, must be modified to

$$J_{1min} = M_{*L}\Gamma_c^2/(2\pi) + J_{EX}, \tag{69}$$

where $M_{*L} = 3.742$ is the minimum value of M in Long's problem and J_{EX} is the contribution of the external flow given by (55).

3.6. *Summary of the asymptotic analysis*

Since the above analysis is rather lengthy, the main asymptotic results will be summarized here. When both flow force J_1 and circulation Γ_c are high enough there are four or five solution branches depending on the cone angle θ_c.

Cone with $\theta_c < 90°$

(i) The flow force J_1 is positive and has two minima and one maximum at a fixed value of Γ_c.

(ii) One of the minima, $J_1 = J_{min1}$ is of $O(\Gamma_c^2 \ln \Gamma_c)$ (see (55), (69)) and occurs in the one-cell regime with the near-axis outflow (Long's jet). This fold relates to vortex breakdown (arrow B in figure 3*d*).

(iii) The maximum $J_1 = J_{max}$ is of $O(\Gamma_c^3)$ (see (35)) and occurs in the two-cell regime with the inner annular outflow (the annular jet). This fold relates to vortex consolidation (arrow C in figure 3*d*).

(iv) The other minimum $J_1 = J_{min2}$ is of $O(\Gamma_c^{3/2})$ (see (43)) and occurs in the one-cell regime with the near-surface outflow.

Cone with $\theta_c > 90°$

(i) At a fixed value of Γ_c, J_1 has two minima and two maxima.

(ii) The same as conclusion (ii) for $\theta_c < 90°$ but now J_{min1} is negative.

(iii) For the first maximum $J_1 = J_{max1}$ is positive see conclusion (iii) for $\theta_c < 90°$.

(iv) The second minimum $J_1 = J_{min2}$ is negative, of $O(\Gamma_c^3)$ (see (35)), and occurs in the two-cell regime with the inner annular outflow directed downward ($x_s < 0$). This fold relates to a jump attachment of the outflow to the cone surface (arrow *A* in figure 3*d*).

(v) The second maximum $J_1 = J_{min2}$ is negative, of $O(\Gamma_c^{3/2})$ (see (43)), and occurs in the one-cell regime with the near-surface outflow (figure 3*c*). This fold relates to a jump separation of the outflow from the cone surface (arrow S in figure 3*d*).

Now we compare our asymptotic results with numerical calculations for a few specific problems and show how the folds disappear as Γ_c decreases.

4. Swirling flows in cones

The Introduction mentions vortex suction devices to remove hazardous fumes from a distant localized region. For instance, during a welding process it is necessary to remove 900–1500 $m^3\,h^{-1}$ of air from a region near an electric arc. Vortex suction can be more effective than a conventional vacuum cleaner owing to the very low pressure created by swirl in the near-axis region. The device creates a long-range 'focused' suction because velocity generated by a momentum source decays as r^{-1} while velocity generated by a mass sink (in typical kitchen suction) decays as r^{-2}. However, vortex suction has an undesirable feature: the possibility of unexpected jumps between flow regimes can lead to blowing on the hazardous fume instead of sucking it out. Keeping in mind this problem and the devices described in §1 we consider two specified cases of the conically similar solutions. First, the flow geometry like that shown in figure 1(*b*) but for a specific value of θ_c (we choose 45° as an intermediate value) is studied.

4.1. *Flow regimes inside the $\theta_c = 45°$ cone*

4.1.1. *Numerical results at $\Gamma_c = 100$.*

We fix swirl at the surface at the rather large value $\Gamma_c = 100$ and consider the dependence of the solutions on the dimensionless flow force J_1. Figure 8 shows the relation between J_1 and $Re_m = rv_{rm}/\nu$, where v_{rm} is the maximal radial velocity at a fixed distance r from the apex. The insets in figure 8 show all typical forms of the radial velocity profiles and the meridional motion patterns. The solid curve in the main plot of figure 8 corresponds to the numerical calculations. The broken lines are asymptotes as $\Gamma_c \to \infty$, which follow from the analytic solutions of §3 (dashed line 1A and the close branch of the solid curve are terminated at $J_1 \approx 10^4$ in figure 8 to avoid a possible confusion at curve intersections). There are four solutions in the range $10490 < J_1 < 17410$, between points B and C, as the asymptotic analysis has predicted.

The asymptotes help to clarify the arrangement and meaning of these four branches of solutions. Asymptote 1A is for the one-cell regime whose typical streamline is shown in figure 1(*b*). For this regime the maximum of the radial velocity occurs at the surface, i.e. $Re_m = Re_c$, and the relation for 1A follows from (50) with $x_c = 1/\sqrt{2}$:

$$Re_m = (9/2)^{1/3} J_1^{2/3}.$$

This corresponds to a strong outflow along the surface and a nearly uniform inflow inside the cone (see the sketch for 1A in figure 8). Swirl is weak compared to the meridional motion. Such a regime is relevant for the above described suction device, but unfortunately is not unique and possibly unstable.

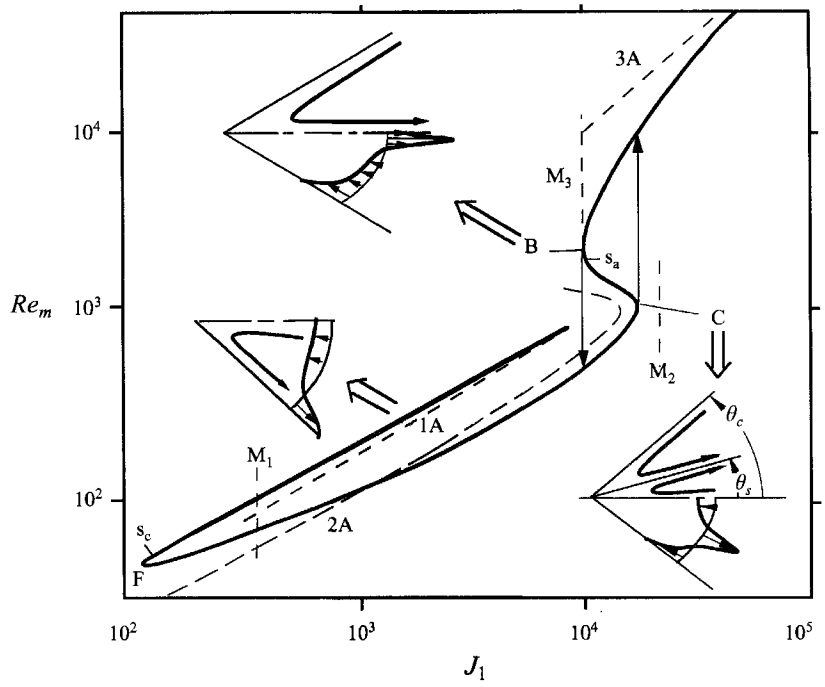

FIGURE 8. Numerical (solid curve) and asymptotic (dashed curves) results for the dependence of the maximal radial velocity Re_m on flow force J_1 for the flow inside cone $\theta_c = 45°$ at $\Gamma_c = 100$. Inset sketches show flow patterns for branch 1A and folds B and C.

The solid curve in figure 8 approaches 1A as $J_1 \to \infty$ and has turning point F at $J_1 = 122$. This value is smaller than $J_{min1} = 410$ calculated using (43) and shown by line M_1 in figure 8. The difference between the numerical and asymptotic results is remarkable because J_1 is rather small at F. The flow separation from the cone occurs at point s_c in figure 8. The next two branches of the solid curve are positioned near asymptote 2A. This asymptote is for the two-cell regime and its equation follows from (19) and (35) with $x_c = 1/\sqrt{2}$:

$$Re_m = \tfrac{1}{2}\Gamma_c^2(x_s - 1/\sqrt{2})^2(1+x_s)^{-2}(1-1/\sqrt{2})^{-2},$$
$$J_1 = \tfrac{2}{3}\Gamma_c^3 x_s(x_s - 1/\sqrt{2})^3(1-x_s)^{1/2}(1-1/\sqrt{2})^{-3}(1+x_s)^{-5/2},$$

where x_s serves as a parameter. The turning point of 2A is closer to the turning point C of the solid curve than F is to M_1 because J_{1max} is significantly larger than J_{min1}. If one takes into account the contribution from the near-surface boundary layer given by (34), then the asymptotic value of J_{1max} increases as shown by line M_2 in figure 7. Therefore, the asymptotic results provide the upper and lower estimates for the numerical value. The nearest inset shows the meridional flow at C.

As one goes from s_c through F and C to turning point B along the solid curve in figure 8, separating angle θ_s (see the sketch near C) decreases from $\theta_s = \theta_c = 45°$ at s_c to $\theta_s = 17°$ at C and becomes zero at point s_a corresponding to jet attachment to the axis. Above s_a, the flow pattern is one-cellular with an inflow near the surface and a strong outflow near the axis (see the sketch for point B).

As $\Gamma_c \to \infty$, the near-axis swirling jet has the limiting pattern of Long's vortex. However, the value of J_{min2} is different from that in Long's jet owing to the

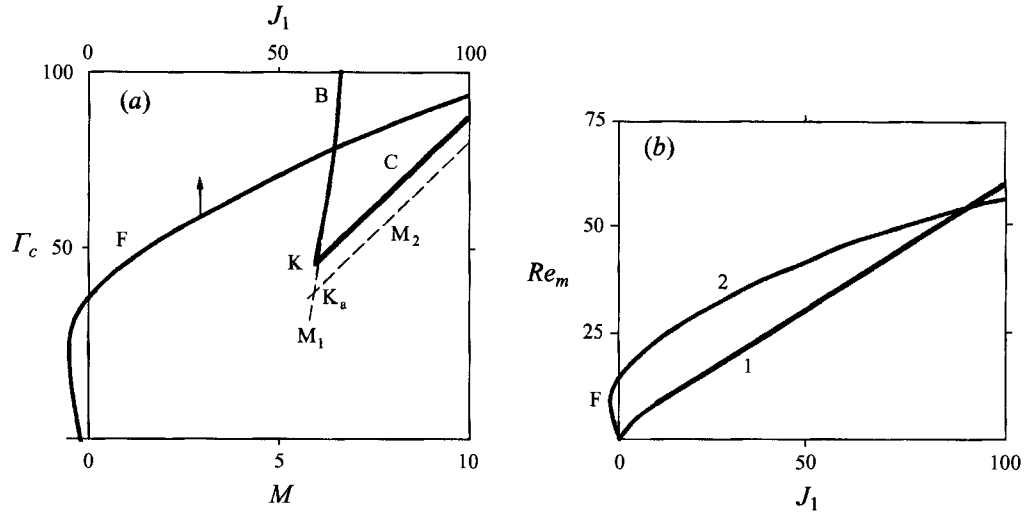

FIGURE 9. (*a*) Numerical (solid curves) and asymptotic (dashed curves) results for folds B, C, and F projected on the control parameter plane. (*b*) Maximal radial velocity Re_m versus flow force J_1 for the swirl-free flow ascending (curve 1) and descending (curve 2) near the axis. $\theta_c = 45°$.

contribution of the external flow. Asymptotic relations (55) and (69) give, for $\Gamma_c = 100$ and $x_c = 1/\sqrt{2}$, the value of $J_{min\,2}$ shown by line M_3 in figure 8. It coincides, within the accuracy of the drawing, with the numerical results for point **B**. The flow regimes in the vicinity of and above point **B** are extremely undesirable for the suction device because they cause spreading of hazardous fumes instead of collecting them.

As $J_1 \to \infty$ along the upper branch of the solid curve in figure 8, the maximum of the radial velocity occurs on the axis, i.e. $Re_m = Re_a$, and swirl becomes weak near the axis compared to the meridional outflow whose pattern approaches that of Schlichting's round jet. Asymptote 3A corresponds to the relation $Re_m = \frac{3}{4}J_1$, which is valid for Schlichting's jet. If one draws curve 1 of figure 7(*b*) in figure 8, then after rescaling and shifting (55), the upper branches of curve 1 and the solid curve in figure 8 would merge within the accuracy of the drawing. Thus, we see good quantitative agreement between the numerical and asymptotic results at $\Gamma_c = 100$. This is a good check for both the calculation methods. The asymptotic theory is not expected to reveal how the folds disappear at small values of J_1 and Γ_c. This seems to be a subject for numerical calculations only.

4.1.2. *Behaviour of the folds at small* Γ_c

Solid curves **B**, C, and F in figure 9(*a*) show projections of the corresponding folds (see figure 8) on the plane (M, Γ_c) for $\Gamma_c < 100$. We use Long's parameter M as the abscissa for a compact presentation of the calculated data. Curves **B** and C in figure 9(*a*) meet and terminate at cusp point K ($\Gamma_c = 45$, $M = 6.8$). Note that M is significantly larger on the entire curve **B** than $M_{*L} = 3.742$. Moreover, there is no finite limit for M as $\Gamma_c \to \infty$ along curve **B**. Dashed curve M_1 in figure 9(*a*) shows the asymptotic relation for fold **B**, $M = 3.19 + 0.74 \ln \Gamma_c$, resulting from (55) and (69) with $x_c = 1/\sqrt{2}$. One can see that **B** and M_1 coincide within the accuracy of the drawing except around K. Dashed curve M_2 shows the asymptotic relation for fold C, $M = 0.0964\Gamma_c + 0.645 \ln \Gamma_c$, resulting from (34) and (35) with $x_c = 1/\sqrt{2}$ and $x_s = 0.9576$. The gap between C and M_2 is mostly due to contributions, to J_1 of $O(\Gamma_c^2)$ from the

inviscid regions $x_c < x < x_s$ and $x_s < x < 1$, which are ignored in M_2. The intersection of M_1 and M_2 gives the asymptotic prediction K_a for the cusp point K.

In contrast to curves B and C that terminate at K, curve F extends up to $\Gamma_c = 0$. This means that for small and even zero swirl, there are two solutions having the same flow force (figure 9*b*). Note that for $\Gamma_c < 40$ the minimum value of the flow force (shown by curve F) is negative. The flow force can be integrated at a section $z = r\cos\theta = \text{const}$:

$$J = 2\pi\rho \int (v_z^2 + p/\rho - 2\nu\,\partial v_z/\partial z)\, s\,\mathrm{d}s = 2\pi\rho\nu^2 J_1, \quad s = r\sin\theta.$$

Since the first term (the contribution of the momentum flux) is positive, the negative value of J_1 means that the contributions of pressure and viscous stresses dominate for $\Gamma_c < 40$.

Figure 9(*b*) shows the relation between J_1 and Re_m at $\Gamma_c = 0$. There are two curves starting from the origin: curve 1 corresponds to the flow pattern with the near-axis outflow (see the sketch for B in figure 8), and curve 2 corresponds to the opposite flow direction (figure 1*b*). The results shown in figure 9(*b*) help us to conjecture on the stability features of the regimes. Since the origin in figure 9 corresponds to fluid at rest, we expect that near the origin both the curves are related to stable regimes. In the vicinity of fold F, where the tangent bifurcation occurs, the general theory says that at least one of the branches corresponds to unstable solutions. If the lower branch of curve 2 corresponds to stable solutions, then the upper branch of curve 2 must correspond to unstable ones.

To test these conjectures, one needs to study the stability and this will be a subject of our future work. Here, having in view only a special class of disturbances that can induce transitions between the above regimes, we assume that the stability of the solutions considered changes at the folds. Then as curve 1 figure 9(*b*) corresponds to the upper branch of the solid curve in figure 8, we assume that solutions are stable for this branch, unstable for branch BC, again stable for CF, and unstable for the branch near 1A.

By applying this consideration to the suction, we see that the flow regime that seems most favourable for suction (figure 1) is unstable. The flow pattern that corresponds to branch CF in figure 8 (see sketch for C) is also quite acceptable for the suction device because there is an inflow near the axis. This regime seems to be stable to small disturbances at least in some range of the flow force. However as J_1 increases, a jump transition can occur from suction to blowing (see the vertical arrow from C in figure 8), and a jump from blowing to suction can occur as J_1 decreases (see the vertical arrow from B in figure 8). Within the bi-stability range (between B and C in figure 8) finite-amplitude disturbances can cause transitions in both directions. Consider a fixed value of J_1 within the bi-stability range. Since solution S_u on the upper branch (i.e. above B) of the solid curve in figure 8 is assumed to be stable, this means that S_u is stable also with respect to small but finite-amplitude disturbances. The difference between solution S_{BC} (corresponding to branch BC) and S_u can be considered as a finite-amplitude disturbance. As this disturbance transforms one steady solution (S_u) to another (S_{BC}), one can consider the difference, $S_{BC} - S_u$, as a kind of neutral disturbance. Therefore, a disturbance of amplitude larger than that of $S_{BC} - S_u$ can cause the transition from S_u to S_{CF} (corresponding to branch CF). Then a disturbance of amplitude larger than that of $S_{BC} - S_{CF}$ can cause the back transition from S_{CF} to S_u.

Such transitions are indeed observed (Spotar' & Terekhov 1987); to avoid them

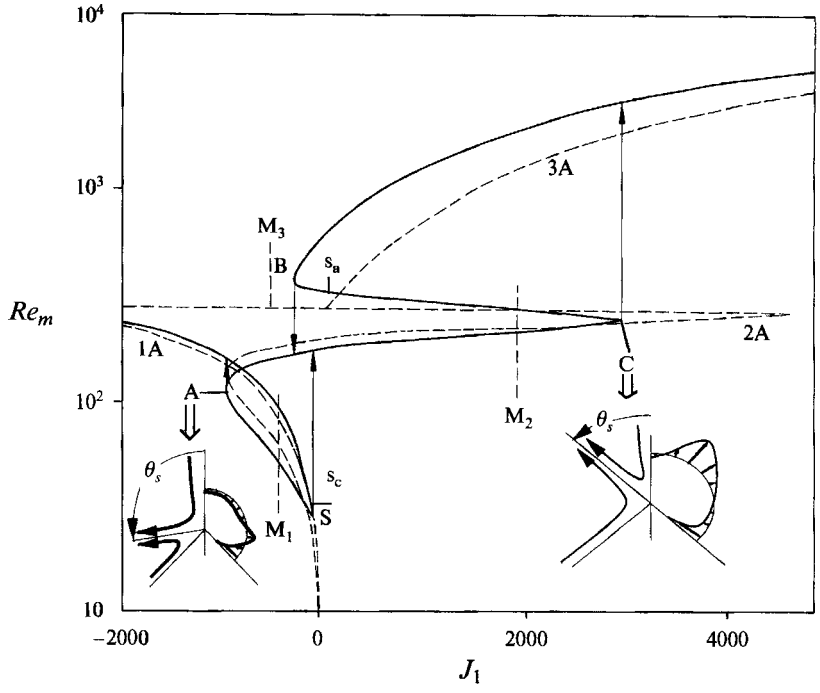

FIGURE 10. Numerical (solid curve) and asymptotic (dashed curves) results for dependence of maximal radial velocity Re_m on flow force J_1 for the flow inside cone $\theta_c = 135°$ at $\Gamma_c = 50$. Sketches show flow patterns for folds A and C.

another version of the suction device was invented (see figure 1*c*). To study flow regimes for this device we consider the next simplified model.

4.2. *Flow regimes outside the* 45° *cone*

4.2.1. *Jump flow separation from the surface*

Although the model considered here differs from that in the previous section only in the angle θ_c (see figure 1*d*), this leads to a very different map of flow regimes. Figure 10 shows the relation between J_1 and Re_m at $\Gamma_c = 50$. Again the solid curve corresponds to the numerical results and the dashed curves are asymptotes similar to those in figure 8 but calculated for $x_c = -1\sqrt{2}$. The drastic difference with the case $x_c = 1\sqrt{2}$ is that the solid curve has now four folds: A, B, C, and S, and the flow force can decrease down to $-\infty$. This occurs as Re_m increases along the branch of the solid curve in figure 10 that is near asymptote 1A. The equation for 1A follows from (50) with $x_c = -1/\sqrt{2}$: $J_1 = -(2^{1/2}/3)\,Re_m^{3/2}$. The flow pattern is like that shown in figure 3(*c*), i.e. there is a strong downflow in the near-surface boundary layer and slow downflow elsewhere. Swirl is weak in comparison with the meridional motion. Such a regime is not favourable for the suction device because the inflow velocity near the axis is small compared to the outflow velocity near the surface and therefore the efficiency of the vortex suction is small.

The solid curve in figure 10 has fold S at $J_1 = -54$. The asymptotic prediction is $J_{min1} = -410$ calculated using (49) and shown by line M_1. The difference between the numerical and asymptotic results is remarkable because $|J_1|$ is small. The flow regime becomes two-cellular at separation point s_c that is close to but above S. The two-cell regimes correspond to asymptote 2A, and the next three branches of the solid

curve are positioned near 2A. The equations for 2A follow from (19) and (35) with $x_c = -1/\sqrt{2}$:

$$Re_m = \tfrac{1}{2}\Gamma_c^2(x_s+1/\sqrt{2})^2(1+x_s)^{-2}(1+1/\sqrt{2})^{-2},$$
$$J_1 = \tfrac{2}{3}\Gamma_c^3 x_s(x_s+1/\sqrt{2})^3(1-x_s)^{1/2}(1+1/\sqrt{2})^{-3}(1+x_s)^{-5/2},$$

where x_s serves as a parameter. If one moves along the solid curve, as J_1 increases from $-\infty$ approaching zero and reaches S, then the jump occurs. This jump, shown by an arrow from S to branch AC, corresponds to the transition from a flow pattern as in figure 3(*c*) to a pattern as in figure 3(*b*). Since J_1 is small and negative, separation angle θ_s is slightly larger than 90° in the final two-cell regime. Therefore, this jump is the abrupt flow separation from the surface causing the angular direction of the outflow to change by nearly 45°.

4.2.2. *Jump flow attachment, vortex consolidation, and vortex breakdown*

If one moves along branch AC of the solid curve in figure 10 as J_1 decreases and reaches turning point A, then another jump transition occurs – shown by the arrow from A to the branch near 1A. The minimum value of J_1 ($= -986$) at A is close to that for 2A and corresponds to the two-cell flow with $x_s = -0.141$. The sketch in the left lower corner of figure 10 shows the flow pattern and distribution of the radial velocity for fold A. This is the initial flow state before the jump attachment of the outflow to the cone, and a final state is the one-cell flow as shown in figure 3(*c*).

The other transitions, vortex consolidation and vortex breakdown related to folds C and B in figure 10, are the same for any value of x_c (see figure 8). Fold C in figure 10 corresponds to the maximum of J_1 that is positive and large: $J_1 = 3092$ at $\Gamma_c = 50$ and $J_1 = 0.0384\Gamma_c^3$ as $\Gamma_c \to \infty$. The sketch in the right lower corner of figure 10 shows the flow pattern and distribution of the radial velocity for point C. The position of the separating cone, $x_s = 0.753$, at C is close to $x_s = 0.747$ as predicted by the asymptotic analysis, but values of J_1 differ significantly for C and the corresponding the turning point of curve 2A in figure 10. The difference is due to a contribution from the outer flow that is neglected for 2A. Line M_2 in figure 10 shows the asymptotic value of $J_{1\,max}$ for which the contribution from the near-surface boundary layer is also included. The difference between M_2 and C is due to the contributions of the potential flow and vortical inviscid flow. Again, the asymptotic results provide the upper and lower estimates for the numerical value.

Regimes corresponding to the vicinity of C along branch AC of the solid curve in figure 10 seem most favourable for the suction device: the inflow occurs in a rather narrow near-axis region with a comparatively large radial velocity (e.g. see the sketch for C in figure 10) that provides the long-range suction needed. Unfortunately, like the $\theta_c = 45°$ case, there is also a possibility of the transition from suction to blowing due to vortex consolidation. However, if a value of J_1 is chosen in the middle part of branch AC (that is large at high Γ_c) then the probability of the jump is smaller.

When one moves along the solid line in figure 10 from C to B, angle θ_s of the separating surface decreases and becomes zero at point s_a. The most striking difference with the $\theta_c = 45°$ case (figure 8) is that now J_1 is negative at B even though the corresponding flow is directed forward with a strong outflow near the axis (Long's jet). Figures 2, 3(*a*) and 7(*a*) show a typical streamline and the distribution of the radial velocity for point B in figure 10. The negative value of $J_1(= -273)$ at B is due to the contribution from the near-surface boundary layer as the asymptotic analysis has shown. Relations (55) and (69) at $x_c = -1\sqrt{2}$ give the value of $J_{min\,2}$ shown by line M_3 in figure 10. The intersection point of asymptotes 2A and 3A ($Re_m = \frac{3}{4}J_1$) together with

M_3 provide the upper and lower estimates for J_1 at B. Although the negative sign of J_1 in the vicinity of B has already been predicted in §3, the following analysis allows us to investigate the nature of this unusual swirling effect in more detail. For this we first study the pressure distribution.

4.2.3. *Strong variation of pressure near the surface*

At first sight, the negative value of J_1 is due to the contribution from the pressure. The pressure distribution near the axis (inside Long's boundary layer) is universal for any x_c; however, pressure profiles outside the Long's jet are qualitatively different for $x_c > 0$ and $x_c < 0$. Substituting (52) in (8) and neglecting the linear terms we get the asymptotic pressure distribution in the inviscid core, $x_c < x < 1$, as $\Gamma_c \to \infty$:

$$q_i = -\tfrac{1}{2}\Gamma_c^2[(x-x_c)-x_c(1-x)]/[(1-x_c)(1-x^2)]. \tag{70}$$

This, in particular, yields the pressure value at the cone surface predicted by the inviscid theory,

$$q_{ci} = \tfrac{1}{2}\Gamma_c^2 x_c/(1-x_c^2). \tag{71}$$

Therefore, when $x_c > 0$, pressure is positive near the surface and provides a positive contribution to the flow force. Since the contribution of the momentum flux is also positive, and the contribution of the shear stresses is negligible for large Γ_c, the flow force is positive in the near-surface boundary layer. This makes the total flow force positive because the contribution of the near-surface region, being $O(\Gamma_c^2 \ln \Gamma_c)$, dominates contributions of the other regions that are of $O(\Gamma_c^2)$. In contrast, q_{ci} is negative for $x_c < 0$.

In the near-surface boundary layer, the linear term $-x\psi''$ in (8) also contributes to the pressure. By using (23) in (8) and allowing $\Gamma_c \to \infty$ we obtain

$$q = -\tfrac{1}{2}\Gamma_c^2(W''-WW')\,x_c/(1-x_c^2).$$

It follows from differentiation of (25) that $W''-WW' = -1$, so that the pressure is constant across the near-surface boundary layer and equals $q_{cb} = \tfrac{1}{2}\Gamma_c^2 x_c/(1-x_c^2)$. Comparison with (71) shows that the inviscid and boundary layer predictions of pressure coincide, in agreement with the general theory (Schlichting 1979).

Figure 11(*a*) shows the pressure distribution corresponding to fold B in figure 10. The solid curve in figure 11(*a*) shows the numerical result at $\Gamma_c = 100$, and the dashed line shows the inviscid solution (70). One can see that the numerical and asymptotic results are very close. On the surface (71) yields $q\Gamma_c^{-2} = -0.707$ and the numerical result is $q\Gamma_c^{-2} = -0.746$. On the axis, the inviscid limit gives $q\Gamma_c^{-2} = -\infty$ (see (70)), but the numerical value is $q\Gamma_c^{-4} = -0.0194$, which coincides with Long's boundary-layer result. The pressure maximum near $x = 0$ has a clear physical reason. The pressure gradient balances the centrifugal force (i.e. cyclostrophic balance); thus pressure drops as the distance from the symmetry axis decreases. On a sphere $r = \text{const}$, $x = 0$ is a position most remote from the axis. As $|x|$ increases, the distance decreases, and pressure drops as figure 11(*a*) shows. At $x_c = -1$, (70) becomes exactly symmetric with respect to $x = 0$: $q_i = -\tfrac{1}{2}\Gamma_c^2/(1-x^2)$. Thus, for cones with $x_c < 0$, pressure drops not only near the axis but also near the surface, and figure 11(*a*) shows that this drop can be significant.

4.2.4. *The nature of 'anti-rocket' thrust*

The negative value of J_1 in the vicinity of point B in figure 10 means that the flow produces a thrust $-J_1$ acting on the cone in the jet direction. This contrasts with the swirl-free jet emitted by a rocket and providing a thrust opposite to the jet direction (we

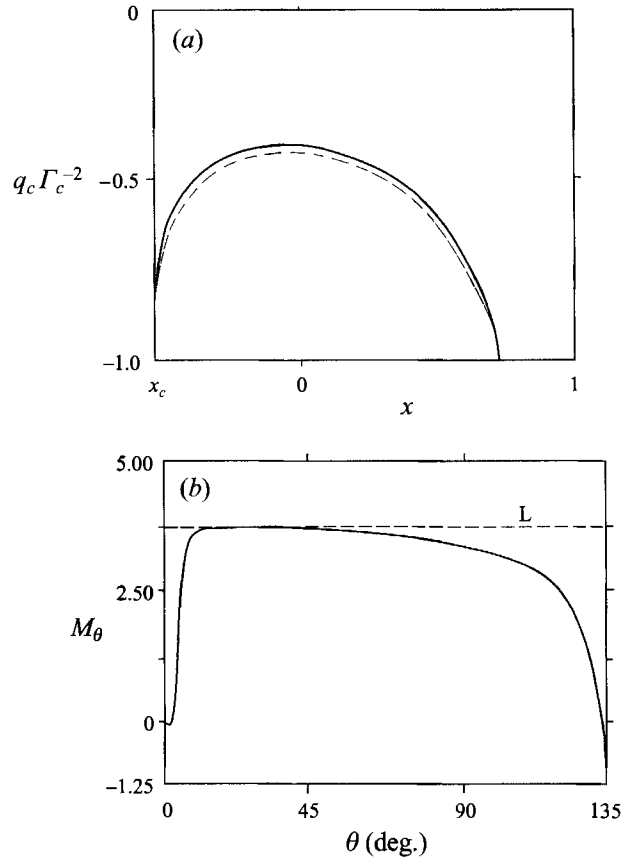

FIGURE 11. Numerical (solid curve) and asymptotic (dashed curve) solutions for (*a*) pressure and (*b*) flow force distributions for fold B in figure 10, but at $\Gamma_c = 100$. Line L in (*b*) shows $M_{*L} = 3.742$ following Long's boundary layer approach.

call this the *anti-rocket* effect). To understand the role of pressure in the negative value of J_1, it is useful to compare distributions of pressure and the flow force. Figure 11(*b*) shows $M_\theta = 2\pi J(\theta)\Gamma_c^{-2}$ versus θ for $\Gamma_c = 100$. Here $J(\theta)$ is a contribution to the flow force from interval $(0, \theta)$, so that $J_1 = J(\theta_c)$. As θ increases, M_θ first drops (due to the pressure contribution), then increases (due to the momentum flux contribution), reaches its maximum (which corresponds to Long's value for the fold, $M_{*L} = 3.742$, shown by dashed line L in figure 11*b*), gradually decreases in the inviscid core, and finally drops steeply in the near-surface boundary layer. The latter drop seems to be related to the pressure drop near $x = x_c$ ($\theta_c = 135°$) in figure 11(*b*). However, it follows from (7) that negative q for negative x gives a positive contribution to j, and therefore a positive contribution to J_1. This means that the direct contribution from the pressure to the flow force cannot provide the 'anti-rocket' effect. The other term of (7), xu^2, yields a negative J_1. Indeed, this term is negative for $x < 0$, and, due to (23), $u = -\psi' \sim O(\Gamma_c^{4/3})$. Therefore, term xu^2 is $O(\Gamma_c^{8/3})$ and larger than q which is $O(\Gamma_c^2)$. Thus J_1 is negative due to the momentum flux.

Nevertheless, the negative pressure (induced by swirl) plays a crucial role in the anti-rocket thrust because the low pressure induces high radial velocities near the surface. In swirl-free jets the radial velocity is bounded: $Re_c = -7.67$ for the Squire jet and $|Re_c|$ decreases as θ_c increases up to $Re_c = -2$ for the Landau jet. The radial velocity u is

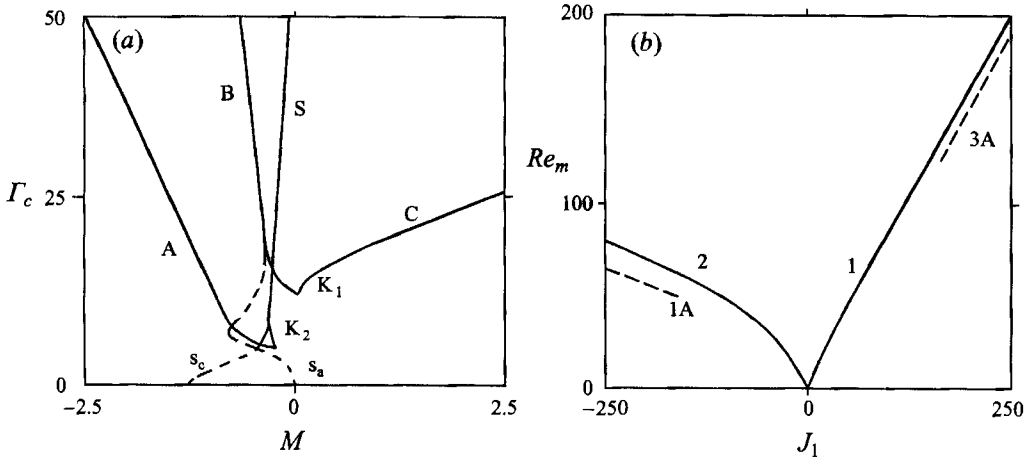

FIGURE 12. (*a*) Numerical results for the control parameter values corresponding to folds A, B, C, and S (solid curves) and flow separation from the axis s_a and the cone s_c (dashed curves). (*b*) Maximal radial velocity Re_m versus flow force J_1 for the swirl-free flow inside cone $\theta_c = 135°$.

small outside the near-axis jet in swirl-free flows. This yields that a positive contribution to the flow force from the near-axis jet dominates a negative contribution from the near-surface region.

An inflow induced by swirl is the well-known 'wall' effect in rotating flows. The reason is that the pressure gradient is not balanced by the centrifugal force at the wall due to the no-slip condition. However, the development of the near-surface jet in our case is different from the wall effect because the no-slip condition is not invoked. It seems paradoxical, but the near-surface jet develops with the impermeability condition as follows from the asymptotic analysis in §3.2.1. The impermeability causes the 'square-root' law for the inviscid stream function near the surface (see, e.g. (52)), i.e. the singularity of the radial velocity. This singularity smoothed by viscosity leads to the strong near-surface inflow. On the other hand, swirl makes the near-axis jet wider and weaker. As a result, a negative contribution to the flow force from SL dominates a positive contribution from Long's jet. Thus owing to the specific geometry ($x_c < 0$) and the swirl action, the flow produces thrust in the direction of blowing.

4.2.5. *Cusp catastrophes*

Curves A, B, C, and S in figure 12(*a*) show projections of the respective folds on plane (M, Γ_c) for $\Gamma_c < 50$. Again we use Long's parameter M as the abscissa for a compact presentation of the calculated data. Curves B and C meet and terminate at cusp point K_1 ($J_1 = -11.34$, $\Gamma_c = 11.8$). Note that M is negative along curve B up to its termination point. For high Γ_c, curve B approaches the asymptote $M = 1.67 - 0.74 \ln \Gamma_c$ that follows from (55) and (69), and curve C approaches the asymptote $M = 0.241\Gamma_c - 0.345 \ln \Gamma_c + 3.77$ derived with the help of (34) and (35). Jump vortex breakdown and consolidation do not occur for $\Gamma_c < 11.8$. In contrast, flow separation and attachment related to changing of flow patterns (*a–c*) in figure 3 exist up to infinitesimal values of J_1 and Γ_c. In particular, transition from the consolidated swirling jet (figure 3*a*) to the two-cell regime (figure 3*b*), which is flow separation from the axis, occurs (at curve s_a in figure 12*a*) for arbitrary small J_1 and Γ_c as well but without jumps and instability.

Curves A and S in figure 12(*a*) meet and terminate at cusp point K_2 ($J_1 = -1.52$, $\Gamma_c = 4.79$). For high Γ_c, curve A approaches the asymptote $M = -0.0473\Gamma_c - 0.67 \ln \Gamma_c$

which follows from (34) and (35). The asymptote for curve S, $M = -2.63\Gamma_c^{-1/2}$, follows from (43). Transition from the one-cell flow (figure 3*c*) to the two-cell regime (figure 3*b*), which can be interpreted as flow separation from the cone, and the opposite transition (flow attachment) occurs (at curve s_c in figure 11*a*) for $\Gamma_c < 4.79$, also without jump and instability.

In the region between curves B and S in figure 12, there are five solutions at each point (M, Γ_c). However, contrary to case $\theta_c = 45°$, here the solution is unique for small Γ_c (below point K2 in figure 12*a*). The numerical calculations of $Re_m(J_1)$ at $\Gamma_c = 0$ (solid curves 1 and 2 in figure 12*b*) together with asymptotes 3A ($Re_m = \frac{3}{4}J_1$) and 1A ($J_1 = -(2^{1/2}/3)\,Re_m^{3/2}$) as $Re_m \to \infty$ (broken curves in figure 12*b*) clearly show the solution uniqueness at any given value of J_1.

Pending a detailed stability study, we can conjecture about stability features of the solutions obtained. Since there are no folds of curves 1 and 2 in figure 12(*b*), the corresponding solutions are expected to be stable. Then using the same arguments as in the case $\theta_c = 45°$, we suppose that the upper branch of the solid curve in figure 10 corresponds to stable solutions, branches BC and AS correspond to unstable solutions, and the remaining branches correspond to stable solutions. These are reasons why each fold in figure 10 relates to a jump transition between regimes in the directions shown by the arrows in the figure. The jump vortex breakdown and consolidation are similar to those found in SH for a tornado model. The two other jumps related to flow separation and attachment are new. Hysteretic transitions related to near-wall separation are not unusual. A well-known example is the so-called 'drag crisis' for flow over a sphere or a cylinder. However, here the jump separation and attachment occur due to the influence of swirl on the near-surface meridional motion.

Thus, our model analysis of the suction devices shows that there is a wide range of flow force and swirl for which the flow pattern is favourable. Inside this region, the favourable flow pattern seems to be stable to small disturbances. However, there are bi-stability and 'tri-stability' (three stable regimes coexisting at the same values of J_1 and Γ_c) in the region, meaning that finite-amplitude disturbances can switch regime to those with undesirable flow patterns. Besides, jump transitions are unavoidable at boundaries of the region. These hydrodynamic features must be carefully taken into account in the design of such devices.

5. A flow driven by a half-line vortex

5.1. *Modification of the flow force*

Now we consider the special case, $x_c = -1$, when the cone collapses to a half-line vortex. This problem is interesting in both its fundamental and applied aspects. It was first studied by Goldshtik (1979) to model outflows of vortex chambers (however, only for small parameter values) and then by Paull & Pillow (1985) and Sozou, Wilkinson & Shtern (1994) as a fundamental problem. There is a difficulty related to the flow force. If one tries to calculate the flow force at a sphere $r = \text{const}$ by applying (7) with $x_c = -1$, then the integral in (7) diverges. The reason is that u has a logarithmic singularity and $u' = -\frac{1}{4}\Gamma_c^2/(1+x) + O(1)$ has a pole at $x = -1$. The divergence is due to term xu' in (8), i.e. the viscous contribution.

There are different ways to overcome this difficulty. Paull & Pillow (1985) removed the singularity by taking the difference between the general flow force and its value for a special problem. However, the physical meaning of this procedure is unclear. The other way is to neglect the viscous terms in (8). This seems to be reasonable for high-speed flows. However, there is the logarithmic singularity for u at any small Γ_c

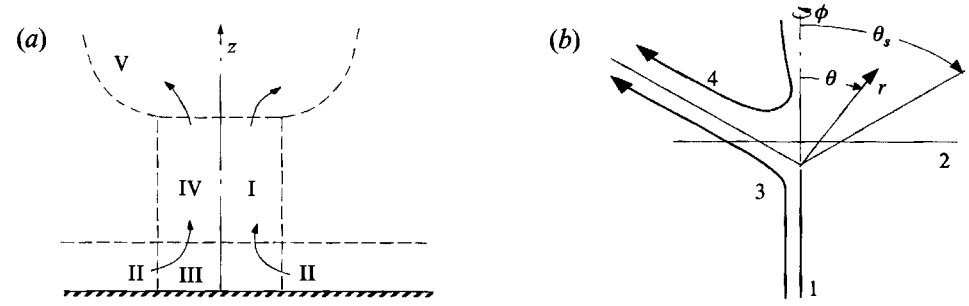

FIGURE 13. (*a*) Schematic of tornado reproduced from Burggraf & Foster (1977) where I is a potential vortex, II is a boundary layer, III is an eruption zone, IV is a vortex core (not to scale), and V is a reverse-flow bubble. (*b*) Model used in the present paper where 1 is a half-line vortex, 2 is a plane where the momentum flux is given, 3 and 4 are typical streamlines of the meridional motion.

excepting $\Gamma_c = 0$ (i.e. Landau's jet). Goldshtik (1979) considered the flow force J_0 acting on a plane $z = \text{const} > 0$ that does not intersect the half-line vortex. A value of J_0 can be found with the help of (7): if J_1 is integrated from $x = 0$ to $x = 1$, then $J_0 = J_1$ (e.g. see SH). The control parameter J_0 is acceptable for swirling jets flowing out from the vortex chamber as in figure 1(*a*). It is not relevant for the case shown in figure 1(*c*) because J_0 does not help to predict the value, or even sign, of the thrust (see §4.2.4).

Another problem where J_0 seems to be relevant is a model of a tornado top that is closely related with Long's formulation. This interpretation of Long's vortex was suggested by Burggraf & Foster (1977, their figure 1 is figure 13*a* here). Similar flow patterns in tornadoes have been reported by Snow (1982) and Davies-Jones (1986). Here we consider a model where the vortex core IV is idealized as a line vortex that terminates at the boundary between IV and the reversed-flow bubble inside region V (figure 13*a*). Also we assume that the ground is far from the bubble, place the reference frame origin at the top of the line vortex, and extend the line vortex to $-\infty$, as figure 13(*b*) shows. Thus we come to the problem formulated in §2 with $x_c = -1$, but now we use $J_0 = \int_0^1 j\,dx$ as the control parameter, where j is defined by (7)–(10). We show below that this problem appears to be an excellent generalization of Long's original formulation for the full Navier–Stoke equations and an infinite domain.

5.2. *Hysteresis*

Here we use a different algorithm from that described in §2.3. The integration runs in both directions from $x = x_s$ with $\psi(x_s) = 0$ and some tentative values of $\Gamma(x_s)$, $\Gamma'(x_s)$, $F(x_s)$, and $F'(x_s)$. Then these values are adjusted by the shooting method to satisfy $\psi(1) = \Gamma(1) = \psi(-1) = 0$ and $\Gamma(-1) = \Gamma_c$. In this procedure, x_s is a free parameter, and then one calculates J_0. Figure 14 shows a typical distribution of stream function (curves 1) and swirl (curves 2) for the two-cell regime with $x_s = 0.71$ at $\Gamma_c = 50$. The solid lines show the numerical results and the dashed lines show asymptotic inviscid solutions (14) and (16) with $x_c = -1$ and $\psi_s = \frac{1}{2}\Gamma_c(1-x_s^2)^{1/2}$, which follows from (16*c*).

One can see that the solid and dashed lines coincide in figure 14 outside the viscous inner layer near $x = x_s$, where analytical solutions $\Gamma = \frac{1}{2}\Gamma_c(1-\tanh\xi)$ and (18) are valid. The product of these solutions with (14) and (16), respectively, coincides with the numerical solutions within the accuracy of the drawing in figure 14. This agreement serves as a check for both numerical and analytical calculations.

Figure 15 shows, for $\Gamma_c = 50$, the numerical (solid curves) and asymptotic (dashed curves) relations between characteristic velocities and J_0. Figure 15(*a*) shows the

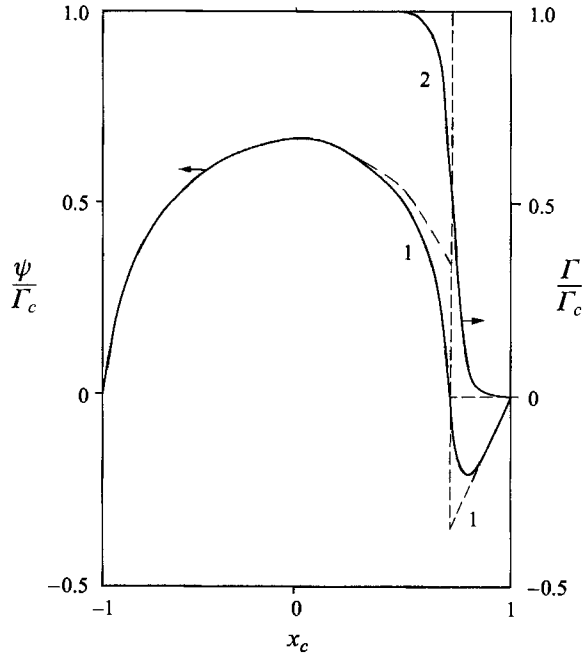

FIGURE 14. Distributions of stream function ψ and circulation Γ for the model shown in figure 13(b) at $\theta_s = 45$ and $\Gamma_c = 50$ (solid curves). Dashed curves are asymptotes as $\Gamma_c \to \infty$.

dependence of $v_m = zv_{\phi max}/\nu$ ($v_{\phi max}$ is the maximal swirl velocity at $z = \text{const} > 0$). Curve 2 corresponds to relation $v_m = \Gamma_c(3J_0/128)^{1/2}$ which is valid for a weakly swirling near-axis jet (SH).

It follows from (29) that

$$J_0 = \Gamma_c^3 x_s(1-x_s^2)^{1/2}/12 \tag{72}$$

and from (14) that $v_m = \Gamma_c x_s/(1-x_s^2)^{1/2}$. Eliminating x_s yields the asymptote $J_0\Gamma_c^{-3} = (v_m/\Gamma_c)/\{12[1+)v_m/\Gamma_c)^2]\}$ shown by curve 3 in figure 15(a). In particular, the asymptote yields that the flow force of the two-cell regimes reaches its maximal value, $J_{0max} = \Gamma_c^3/24$, at $\theta_s = 45°$ with $v_m = \Gamma_c$.

Figure 15(b) shows the maximal radial velocity u_m. For the case considered, $x_c = -1$, the asymptotic value u_m for the annular jet does not depend on x_s and J_0. Relation (19) yields $u_m = 1/8$ which corresponds to dashed curve 3 in figure 15(b). The numerical results for two-cell regimes are quite close to this asymptote. As x_s increases, u_m also increases, and in the one-cell regime the maximum of the radial velocity occurs at the axis (above the cross on curve 1 in figure 15(b). Dashed line 2 corresponds to relation $u_m = 3J_0/4$.

Figure 15(c) shows the velocity at the axis, u_L. If one moves down from the cross on curve 1, then u_L changes its sign below fold B. This means the appearance of an inflow near the axis. After u_L passes its minimum, it increases monotonically as x_s decreases. We stop our calculations when x_s reaches zero because J_0 is not a relevant characteristic for a downward jet. The dashed curve in figure 15(c) corresponds to asymptotic relations (64) and (67). The results for Long's boundary layer (see figure 7b and 7c) agree with those shown by the solid curves in figure 15(b, c). They coincide within accuracy of the drawing (in the scales of figure 15) up to near point C in figure 15. Fold C and the solid curves after C in figure 15(a–c) cannot be revealed in Long's boundary-layer approach. However, values of J_0 are in excellent agreement within a wide area

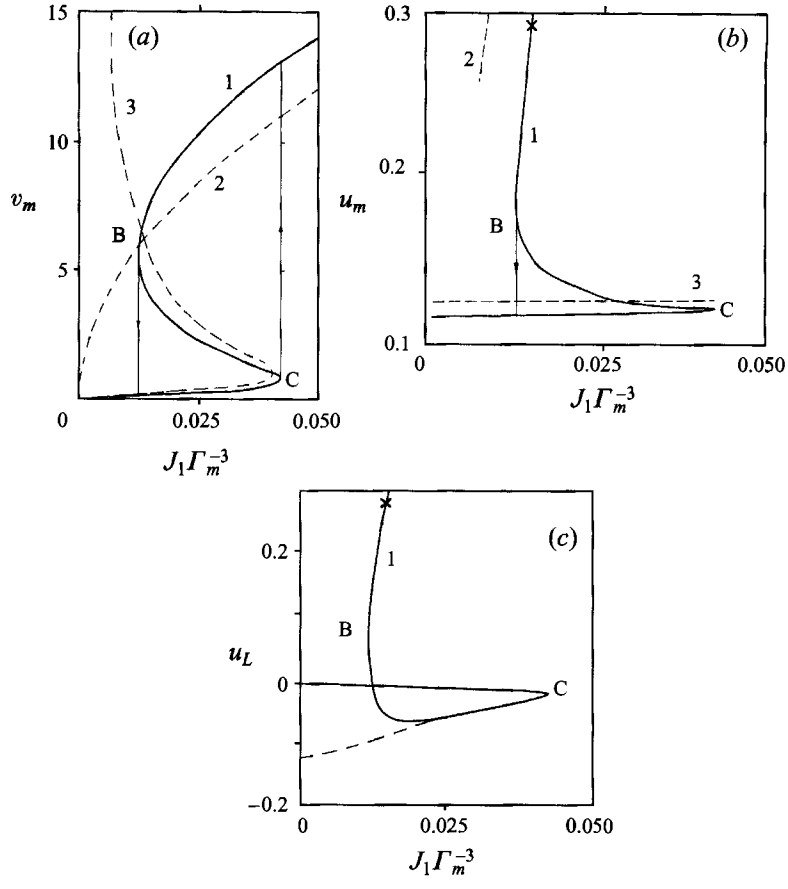

FIGURE 15. Numerical (solid curves) and asymptotic (dashed curves) results for dependence on the flow force of (*a*) maximal azimuthal, (*b*) maximal radial, and (*c*) axial velocities.

around fold B. Before explaining this agreement, which contrasts with the results of §4, we study how the hysteresis disappears.

5.3. *Cusp*

Curves B and C in figure 16(*a*) show projections of the corresponding folds on parameter plane (M, Γ_c). The use of Long's parameter M helps us not only to compactly present the data but also to emphasize the good agreement with Long's case. As Γ_c decreases, curves B and C meet and terminate at cusp point K ($M = 3.05$, $\Gamma_c = 11.5$). Near the cusp point, figure 16(*b*) shows how the folds appear as the swirl increases: the values of $\Gamma_c = 11$, 11.5, and 12 (curves 1–3) would correspond to horizontal lines in figure 16(*a*) passing below, through, and above point K, respectively. Thus we have a generic cusp catastrophe (Arnol'd 1984).

As Γ_c increases, curves C and B tend to their asymptotes – dashed lines 1 and 2 in figure 16(*a*). Line 1 corresponds to the asymptote for curve C, $M = \pi\Gamma_c/12$, which is equivalent to (72) with $x_s = 1\sqrt{2}$. Line 2 is Long's limit, $M = M_L = 3.742$, for fold B. In contrast to the tornado model considered in SH and the models of vortex suction in §4, there is no gap between curves B and 2 as $\Gamma_c \to \infty$ in figure 16(*a*). There the gap was due to a contribution from the outer flow in the flow force. To understand the difference, we have to consider the contribution in this case. The outer flow for Long's

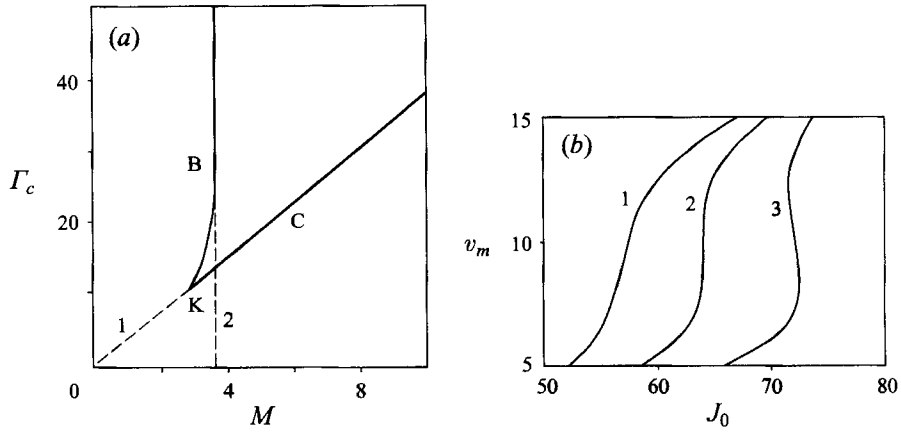

FIGURE 16. (*a*) Numerical (solid curves) and asymptotic (dashed curves) results for folds *B* and *C* (see figure 15) projected on the control parameter plane. (*b*) Dependence of the maximal azimuthal velocity on flow force at $\Gamma_c = 11$ (curve 1), 11.5 (2), and 12 (3), i.e. below, through, and above cusp point K in (*a*).

jet is vortical. To find its contribution to J_0, we have to integrate j in the interval $0 \leqslant x < 1$. For the particular values $x_c = -1$ and $x_s = 1$ corresponding to line 2 in figure 16(*a*), (52) yields

$$\psi = \psi_1 = \Gamma_c(1-x_s^2)^{1/2}/\sqrt{2}.$$

By substituting the latter relation in (9) we find that $j_n \equiv 0$. This means that Long's solution constructed for the near-axis boundary layer is also valid arbitrarily far from the axis on plane $z = \text{const} > 0$ for the problem considered. Therefore, this problem seems to be the most adequate generalization of Long's problem for whole space and for the full Navier–Stokes equations.

6. Pressure peak in swirling annular jets

Finally, we consider one more intriguing feature of swirling jets related to an unusual pressure distribution. Substituting (16) in (8) and keeping only terms of $O(\Gamma_c^2)$, we find

$$q_1 = -\Gamma_c^2\{(x_s-x_s^2)\,x-[2x_s-(1+x_s)\,x_c]\,x_c\}/[(1+x_s)(1-x_c^2)(1-x^2)], \tag{73}$$

$$q_2 = -\Gamma_c^2(x_s-x_c^2)/[(1+x)(1-x_c)^2(1-x_s^2)]. \tag{74}$$

It follows from (73) and (74) that

$$q_1(x_s) = q_2(x_s) = -q_{s0} = -\Gamma_c^2(x_s-x_c^2)/[(1+x_c)(1-x_c)^2(1-x_s^2)].$$

This means that the inviscid solution for pressure is continuous at $x = x_s$ despite the jump in the stream function. According to (74), pressure decreases as one moves from the axis, $x = 1$, to the separating cone, $x = x_s$. Now we show that this decrease is followed by a large pressure peak in the annular jet.

Inside the viscous annular jet, (8) can be reduced to

$$q = q_j = -[x_s F'(x_s) + \psi^2]/(1-x_s^2), \tag{75}$$

where only terms of $O(\Gamma_c^2)$ are taken into account. Subscript j denotes that this solution

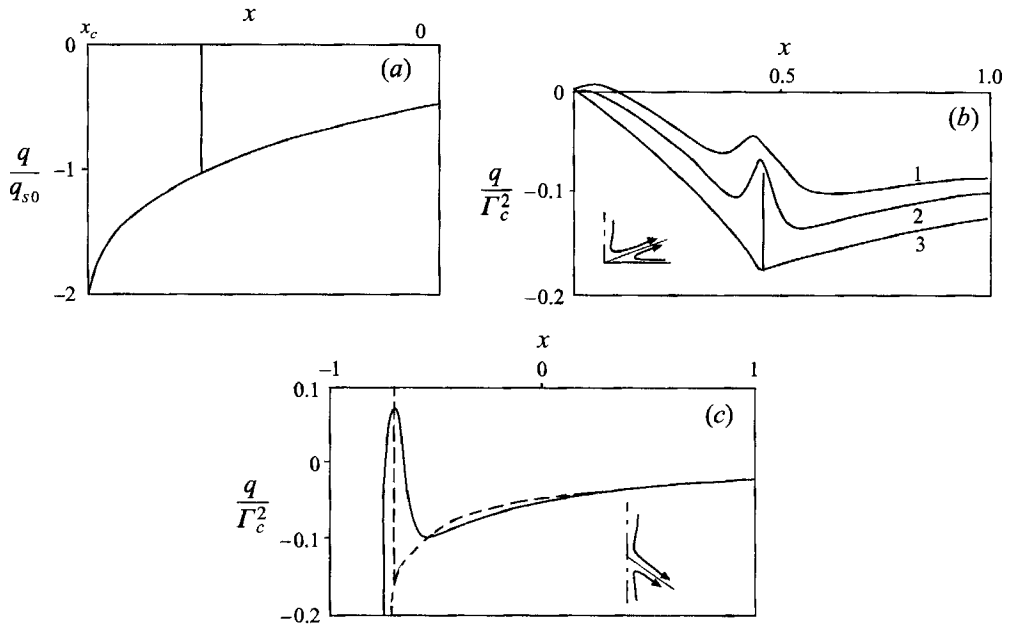

FIGURE 17. (*a*) Asymptotic solution for the pressure distribution with the angle at $x_s = 0$. Pressure distributions at (*b*) $x_c = 0$ and $x_s = 0.452$ for $\Gamma_c = 100$ (curve 1), 200 (2), and ∞ (3); and (*c*) $x_c = -1$ and $x_s = -0.707$ for $\Gamma_c = 50$ (solid curve, numerical) and $\Gamma_c = \infty$ (dashed curve, asymptotic).

is valid inside the jet. We have used in (75) that $F'(x)$ is continuous at $x = x_s$ and can be treated as the constant $F'(x_s) = \psi_s^2/(1-x_s)$ across the annular jet. Also, x can be replaced by x_s inside this jet. Substitution of ψ from (18) transforms (75) to

$$q_j = -\psi_s^2[x_s + (1-x_s)\tanh^2\xi]/[(1-x_s^2)(1-x_s)]. \tag{76}$$

It follows from (76) that pressure varies strongly across the jet, increasing from its value $q = -q_{s0}$ outside the annular jet to its maximum $q = q_{jm} = -x_s q_{s0}$ at $\xi = 0$. The pressure difference,

$$\Delta q = q_{jm} + q_{s0} = (1-x_s)\, q_{s0} = \Gamma_c^2(x_s - x_c^2)/[(1+x_c)(1-x_c)^2(1+x_s)],$$

is of $O(\Gamma_c^2)$. This means that $\Delta p \sim K^2$ and therefore $r^2\Delta p/(\rho K^2)$ is a finite non-zero quantity in the inviscid limit. This contrasts with the fact that pressure variations in swirl-free jets (and SL, see §4.2.3) is a viscous effect: $r^2\Delta p/J$ vanishes in the inviscid limit.

In the particular case of the swirling jet fanning along the plane $x_s = 0$ the solution for pressure is especially simple,

$$q_1 = q_2 = -q_{s0}/[(1+x), \quad q_i = -q_{s0}\tanh^2\xi, \quad q_{s0} = \Gamma_c^2 x_c^2/(1-x_c)^2,$$

and shown in figure 17(*a*). Figure 17(*b*, *c*) shows examples of the pressure distribution for positive and negative x_s. Curves 1–3 in figure 17(*b*) ($x_c = 0$, $x_s = 0.452$) relate to $\Gamma_c = 100$, 200 and ∞, respectively. One can see how the pressure peak increases with Γ_c. In figure 17(*c*) ($x_c = -1$, $x_s = -0.707$), the maximum pressure is positive inside the viscous annular jet while pressure is negative outside it due to the swirl action.

To illuminate the physical nature of this pressure peak, we consider the meridional projection of the momentum equation (i.e. the Navier–Stokes equations for v_θ) in the form

$$r^{-2}\,\partial/\partial r(r^2\Pi_{r\theta})+(r\sin\theta)^{-1}\,\partial/\partial\theta(\sin\theta\Pi_{\theta\theta})=0, \tag{77}$$

where $$\Pi_{\theta\theta}=\rho v_\theta^2+p-2\rho\nu r^{-1}(\partial v_\theta/\partial\theta+v_r)=(\rho\nu^2/r^2)\,[q+(\psi^2-2x\psi)/(1-x^2)], \tag{78}$$

and $\Pi_{r\theta}$ is presented in §2.3. The conical similarity yields that the first term in (77) is zero and, therefore, $\Pi_{\theta\theta}\sin\theta$ does not depend on θ. Since the annular-jet thickness $\delta\theta\sim\Gamma_c^{-1}$, $\Pi_{\theta\theta}$ is constant across the jet in the limiting case $\Gamma_c\to\infty$. Taking into account only terms of $O(\Gamma_c^2)$ in (78) one has $q+\psi^2/(1-x_s^2)=\text{const}$, which is equivalent to (75). This means that $\rho v_\theta^2+p=\text{const}$. Thus, the meridional component of the flow force is invariant, and this produces the pressure peak. Since $v_\theta^2=v_{\theta s}^2$ is not zero at the jet boundary and becomes zero at $\xi=0$, pressure has a peak of height $\rho v_{\theta s}^2$ and $p=p_{\max}-\rho v_\theta^2$, where p_{max} is the maximum pressure at $\xi=0$.

This result does not contradict the boundary-layer theory of jets where the pressure gradient is neglected. In the equation for the radial component of momentum, the pressure term can be omitted because it is of $O(\Gamma_c^2)$ while other terms are of $O(\Gamma_c^4)$. Nevertheless, the variation of pressure inside the jet can be larger than that in the outer inviscid flow. Thus, the pressure peak is a viscous effect despite the fact that the peak height has a bounded non-zero value in the inviscid limit. This effect is one more example of the so-called 'trigger' action of viscosity when even the mere presence of viscosity is crucial.

7. Discussion

7.1. *The physical nature of the jumps*

Our asymptotic analysis and numerical calculations show four kinds of jump transitions in swirling flows: vortex breakdown B, vortex consolidation C, flow separation S, and flow attachment A. These transitions can be identified in the flow by varying a parameter, namely the flow force J_1. Although the choice of J_1 as a control parameter has a reasonable physical background (see §1.3), it is convenient in this discussion to consider a different parameter to explain the nature of the non-monotonic behaviour of J_1 and its physical implications. Control parameters varying monotonically in the solution manifold are suitable for this purpose. In particular, the velocity components at the surface are such parameters since there is a unique solution (of the conical class) for given values of Γ_c and Re_c (Goldshtik & Shtern 1990). From this solution one can find J_1 and study the features of the corresponding surface in parameter space (Γ_c, Re_c). To examine why $J_1(\Gamma_c, Re_c)$ is not a monotonic function, it is convenient to fix one of the arguments, say Γ_c, and consider the dependence of J_1 on the other. However, while this is mathematically tractable, the use of Re_c as a control parameter is not physically appropriate to study the mechanism of transitions B and C. This is because Re_c characterizes the velocity at the surface, i.e. away from the near-axis jet, while most variation of J_1 comes from the jet. It is more relevant to take a control parameter characterizing the jet itself and varying monotonically near folds B and C.

For Long's fold (B) we use the maximum radial velocity v_{rm} as the control parameter. A dominant contribution to J_1 is from the momentum flux, $v_{rm}^2 S_j/(2\pi\nu^2)$, where S_j is the area of a jet cross-section projected on a normal-to-axis plane; see (7). For Schlichting's jet, $S_j\sim\delta^2\sim 1/v_{rm}$ resulting in $J_1\sim v_{rm}$ (see (62)). Therefore J_1

decreases with v_{rm} until swirl does not change the meridional motion. However, when v_{rm} becomes small enough (e.g. in the vicinity of point B in figure 9), the centrifugal forces cause the jet to spread. This increase in S_j is not compensated by a decrease in v_{rm} because v_{rm} is nearly constant (see (63)). As a result, J_1 starts to increase while v_{rm} continues to decrease. Therefore, the minimum of J_1 in Long's vortex is a result of the spreading of the jet by swirl. This prevents a continuous transformation of the near-axis jet into a two-cell flow when J_1 is a control parameter and J_1 decreases; thus, a jump vortex breakdown occurs.

The second extremum (C) of the flow force occurs when θ_s becomes sufficiently large to decrease the projection area. As θ_s approaches 90° (i.e. x_s approaches 0), both $S_j \sim 2\pi\delta r \cos\theta_s$ and J_1 approach zero (see (35)). Therefore, J_1 increases as θ_s starts to increase from zero, but J_1 decreases as θ_s approaches 90°. The maximum of J_1 in the two-cell flow is due to a change in the jet direction from nearly parallel to nearly normal to the axis. For this reason, transformation of the two-cell flow into a near-axis jet is not continuous when J_1 is a control parameter and J_1 increases, i.e. vortex consolidation occurs also by a jump.

The third extremum (A) is caused by reasons similar to those for the second one. The difference is that J_1 is negative because the jet is directed downward at A. Initially, $|J_1|$ increases with $(\theta_s - 90°)$ due to an increase of S_j. However, when the jet approaches the surface $\theta = \theta_c$, v_{rm} starts to decrease rapidly through strong momentum diffusion across the counter-flow. Relation (19) shows that v_{rm} is proportional to $(x_s - x_c)^2$. This causes $|J_1|$ to decrease as $\theta_s \to \theta_c$ and so the transformation of the two-cell flow into the near-surface jet is not continuous when $|J_1|$ increases. In other words, the jet attachment to the surface is abrupt, like the other transitions discussed above.

The fourth extremum (S) occurs when the jet is attached to the surface. For this one-cell regime with the jet flowing out near the surface, Re_c is a relevant control parameter. As Re_c goes to infinity, $|J_1| \to \infty$ as well. Since swirl becomes negligible as $Re_c \to \infty$, (50) becomes valid. Therefore, as Re_c grows, $|J_1|$ decreases and increases before and after the attachment, respectively. This minimum of $|J_1|$ occurs due to the opposed flow forces of the meridional flow and swirl – an effect similar to that in Long's vortex. A high-speed radial jet attracts the ambient fluid (the ejection mechanism) while swirl repels the fluid away by the centrifugal force. For this reason, the separation of the swirling flow from the surface occurs by a jump too.

Thus, the non-monotonic behaviour of J_1 has clear physical reasons. Knowing this behaviour is important for understanding why jump transitions occur in swirling flows. Also this knowledge can help to optimize the flow force of vortex devices, e.g. to design suction devices with minimal J_1. Our results seem useful for such applications despite the approximation of realistic flows by conical ones. We expect that the similarity used in our study to ease the analysis is not crucial for the observed effects (e.g. the jump transitions, anti-rocket thrust and pressure peak) because their physical reasons revealed here are valid for non-similar flows as well. (Besides, one may use a local similarity approximation for non-similar flows.)

Now, based on the relations obtained for the flow force, we will discuss the reasons for stagnation point propagation upstream when vortex breakdown occurs.

7.2. *Dynamics of stagnation points*

In the initial stages of a tornado's life, a funnel propagates downward to the ground from the tornado's cloudbase (Davies-Jones 1982). We model this phenomenon (see the schematic in figure 18*a*) by using a reference frame with its origin at the tip of the funnel and idealizing the funnel shape by a cone with the included angle $\theta = \theta_c$ (figure

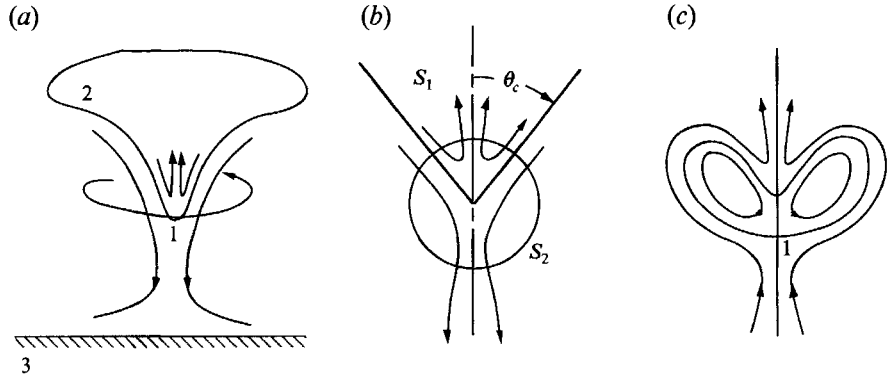

FIGURE 18. (*a*) Schematic of a tornado funnel 1 with cloudbase 2 approaching the ground 3; (*b*) model of (*a*); (*c*) schematic of recirculation bubble with the rear stagnation point approaching the front stagnation point (Wu Wei 1994, personal communication).

18*b*). The coordinate frame moves with the tip velocity, which is taken to be a constant. Also we assume that the air flow from either side of the cone, $\theta = \theta_c$, but outside a spherical region centred at the funnel tip can be approximated by the similarity solutions. The surface of the spherical region consisting of parts S_1 and S_2 (placed inside and outside $\theta = \theta_c$ respectively) is considered as the boundary of the non-similar region near the origin. For a strong swirl, Long's-type vortices develop in both regions, $\theta < \theta_c$ and $\theta > \theta_c$. The force acting on S_1 is directed downward and can be estimated by using (55). Owing to the anti-rocket thrust (see §4.2.4), the force acting on S_2 is also directed downward and can also be estimated using (55). Thus the total force acting on the sphere is given by

$$J = (2\pi x_c/3)\rho K^2 \ln \Gamma_c.$$

As a rough estimate of J in a tornado, we take $x_c = 1$ (because the funnel angle is small at this stage), $\rho = 1$ kg m^{-3}, $K = 10^3$ m^2 s^{-1} (Davies-Jones (1982) gives K from 5×10^3 to 5×10^4 m^2 s^{-1} for mature tornadoes with lower circulation at early stages of the tornado's growth) and $\Gamma_c = K/\nu = 100$ (Burggraf & Foster 1977). This shows that a tornado funnel acting as a 'cumulative shell' could hit the ground with a force $J \sim 10^7$ kg m s^{-2}.

This force driving the stagnation point downstream in the flow geometry shown in figure 18(*b*) may also be a reason for the special deformation of the separation bubble; such deformations have been observed in the temporal evolution of vortex breakdown in a pipe using numerical calculations of the unsteady axisymmetric Navier–Stokes equation (Wu Wei 1994, personal communication). The rear stagnation point of the bubble tends to reach the front stagnation point, as figure 18(*c*) shows schematically. This effect is qualitatively similar to the dynamics of a tornado funnel and agrees with our results.

7.3. *Folds in the context of vortex breakdown theories*

Consider folds A, B, C, S, and the corresponding jump transitions in the context of existing theories for vortex breakdown. The notion of vortex breakdown that originates from experimental observations is that it is characterized as an abrupt increase in the core diameter of a slender vortex filament (Saffman 1992). Different theories emphasize different aspects of the phenomenon: the *abrupt* increase in core diameter and the *failure of the quasi-cylindrical approximation* (or boundary-layer approach) as in the near-wall flow separation (Hall 1972); the appearance of a

stagnation point and the role of *instability* (Leibovich 1984); the analogy with hydraulic jumps and the relation to *inertial wave propagation* (Squire 1956; Benjamin 1962; Keller 1994).

All these aspects are present in our particular problem and the solutions obtained. The folds imply a failure of conical similarity because the transitions (e.g. shown by the arrows in figure 10) cannot be described by similarity solutions. The analogy with Hall's approach can be developed further if one considers quasi-conical flows such that ψ, L, and q depend weakly on r in (1). This 'weak' dependence on r is analogous to the dependence on the streamwise coordiante in boundary-layer theory. For such flows, the arrows in figure 10 may be interpreted as transitions from one quasi-conical flow (upstream flow) to another (downstream flow). However, the transitions themselves are 'strongly' non-similar.

The jump transitions are related to a flow reversal either near the axis (B and C) or near the surface (A and S); and hence, the stagnation points must be within the transition regions. In these situations, both the axial velocity and the azimuthal vorticity ω_ϕ change sign along the axis. One may prefer to use a criterion based on vorticity since ω_ϕ is invariant with respect to a moving frame, and such a criterion is analogous to the one based on shear stress in near-wall separation and attachment. However, ω_ϕ can change sign before the transition. For example, as one moves down along the upper branch of curve 1 in figure 15(*b*, *c*) approaching B, ω_ϕ changes its sign at the cross that is beyond B. Thus, the change in the vorticity sign seems to indicate that the corresponding regime is close to breakdown or separation.

Although instability has not been studied here, the general theory claims that if one of the fold branches corresponds to stable solutions then the other corresponds to unstable ones (Arnol'd 1984). Also, solutions on both branches can be unstable. In particular for Long's vortex, both branches have been found unstable with respect to helical disturbances (Foster & Duck 1982, also see Khorami & Triveli 1994 and references therein). However, there is a special disturbance ('switching' mode) related to the transition between the branches. The stability features of the branches are different with respect to this disturbance. This special instability is most interesting in the context of our paper. Besides, the 'switching' instability also occurs for rather small Γ_c (just above the cusps in figures 9*a*, 12*a* and 16*a*) while the helical instability has been found for larger Γ_c. The directions of jumps shown by arrows (e.g. in figure 10) correspond to our conjectures regarding the stability/instability of solution branches. For example, the upper branch in figure 10 to the right of arrow C seems to be stable with respect to the switching disturbance of an arbitrary amplitude. However to the left of the arrow, the upper branch solutions are stable only with respect to small-amplitude disturbances.

This stability aspect is close to the concept of the *critical states*. According to Squire (1956), a flow in the critical state can support an infintesimal standing wave. Benjamin (1962) showed that the flow force, treated as a variational functional for inviscid flows, has zero values of the first and second variations at the critical state. Keller (1994) found that there are different kinds of transitions corresponding to the sign of the third variation. In a multi-stability region (e.g. in figure 10) differences between solutions corresponding to the same value of J_1 and Γ_c may be considered as neutral standing finite-amplitude disturbances switching between steady solutions. As one approaches a fold, there is a standing disturbance whose amplitude tends to zero. Therefore, the folds correspond to the critical states (Saffman 1992). Besides, the jumps, related to maxima and minima of the flow force in figure 10, may correspond to the classification used by Keller. Since the controlling parameters are the same for flow regimes before

and after the jumps, these regimes may be considered as *conjugated states* (Benjamin 1962).

Our results show that the jump vortex breakdown and flow separation from the axis occur at nearly the same values of the flow force for a strong swirl (see figure 12*a* where curves s_a and **B** merge as $\Gamma_c \to \infty$). This supports the point by Stuart (1987) that the above theories of vortex breakdown are more complementary than competitive.

For small Γ_c, however, changes in the flow pattern occur without any jumps and, presumably, without any instability. For example, figure 12(a) shows 'separation' curves s_c and s_a for flows inside the $\theta_c = 135°$ cone. The flow is ascending (figure 3*a*) to the right of curves s_a, two-cellular (figure 3*b*) between s_c and s_a, and descending (figure 3*c*) to the left of curve s_c. When Γ_c decreases below the level of both cusps K_1 and K_2, there are no jump transitions but flow separation occurs for arbitrarily small Γ_c. As $\Gamma_c \to 0$, $J_1 = (2\pi)^{-1} M\Gamma_c^2 \to 0$ along both s_c and s_a. Therefore, even the extremely slow flow has different flow patterns as the control parameters change. We do not expect any instability for these slow motions. Thus, the jump transitions, flow separation and instability are different phenomena although they can occur together.

We conclude that vortex breakdown is a fold catastrophe. This approach incorporates valuable features but is free of the serious limitations of the prior theories discussed above. The 'abruptness', previously used as a qualitative criterion of vortex breakdown, now becomes mathematically rigorous in terms of the fold catastrophe. The definition based on the fold makes vortex breakdown distinct from the gradually developing internal separation or supercritical instabilities in swirling flows. The fold approach also covers jump vortex consolidation while wave theory deals with vortex breakdown only. Wave theory considers vortex breakdown to be similar to shock waves and hydraulic jumps. However, the opposite jumps are impossible for shock waves and hydraulic jumps but do occur for vortex breakdown. Finally, the fold approach predicts the disappearance of vortex breakdown (through a cusp catastrophe) as swirl decreases.

8. Conclusions

(i) Solution non-uniqueness and hysteresis are found for the conical swirling viscous flows inside a cone, which model vortex suction devices and tornadoes.

(ii) The asymptotic analysis shows the existence of four or five solution branches conneced by folds, depending on the flow force, circulation and cone angle. This is supported by numerical calculations at small and moderate values of J_1 and Γ_c.

(iii) The folds are related to four kinds of jump transitions: vortex breakdown, consolidation, flow separation from the cone surface, and flow attachment to the surface.

(iv) A pressure peak of $O(\Gamma_c^2)$ inside a swirling annular jet is discovered.

(v) The possibility of a swirling jet with anti-rocket thrust is found.

(vi) The physical nature of the jumps is explained and discussed within the context of the prior theories of vortex breakdown. We deduce that vortex breakdown is a fold catastrophe.

This research has been supported by the Air Force Office of Scientific Research Grant F49620-95-1-0302. The authors are grateful to Michael Goldshtik, Jinhee Jeong and Shashi Menon for discussion and reviews of the manuscript.

REFERENCES

ARNOL'D, V. I. 1984 *Catastrophe Theory*, p. 5. Springer.

BENJAMIN, T. B. 1962 Theory of vortex breakdown phenomenon. *J. Fluid Mech.* **14**, 593–629.

BERAN, P. S. & CULICK, F. E. C. 1992 The role of non-uniqueness in the development of vortex breakdown in tubes. *J. Fluid Mech.* **242**, 491–527.

BOGUSLAVSKII, E. M. & IVANSKII, V. G. SU Patent 1542544 A1, 02.12.1987.

BURGGRAF, O. R. & FOSTER, M. R. 1977 Continuation or breakdown in tornado-like vortices. *J. Fluid Mech.* **80**, 685–704.

DAVIES-JONES, R. P. 1982 Tornado dynamics. In *Thunderstorms: A Social, Scientific and Technological Documentary* (ed. E. Kessler), vol. 2, pp. 297–361.

DRAZIN, P. G., BANKS, W. H. H. & ZATURSKA, M. A. 1995 The development of Long's vortex. *J. Fluid Mech.* **286**, 359–377.

FERNANDEZ DE LA MORA, J., FERNANDEZ FERIA, J. & BARRERO, A. 1991 Theory of incompressible conical vortices at high Reynolds numbers. *Bull. Am. Phys. Soc.* **36**, 2619.

FOSTER, M. R. & DUCK, P. W. 1982 Inviscid instability of Long's vortex. *Phys. Fluids* **25**, 1715–1718.

FOSTER, M. R. & JACQMIN, D. 1991 Non-parallel effects in the stability of Long's vortex. *J. Fluid Mech.* **244**, 289–306.

FOSTER, M. R. & SMITH, F. T. 1989 Stability of Long's vortex at large flow force. *J. Fluid Mech.* **206**, 405–432.

GOLDSHTIK, M. A. 1960 A paradoxical solution of the Navier–Stokes equations. *Appl. Math. Mech. (Sov.)* **24**, 610–621.

GOLDSHTIK, M. A. 1979 On swirling jets. *Fluid Dyn.* **14** (1), 19–26.

GOLDSHTIK, M. A. 1981 *Vortex Flows*. Novosibirsk: Nauka.

GOLDSHTIK, M. A. 1990 Viscous flow paradoxes. *Ann. Rev. Fluid Mech.* **22**, 441–472.

GOLDSHTIK, M. A. & SHTERN, V. N. 1990 Collapse in conical viscous flows. *J. Fluid Mech.* **218**, 483–484.

GOLDSHTIK, M. A., SHTERN, V. N. & YAVORSKY, N. I. 1989 *Viscous Flows with Paradoxical Features*. Novosibirsk: Nauka.

HALL, M. G. 1972 Vortex breakdown. *Ann. Rev. Fluid Mech.* **4**, 195–218.

HASAN, M. A. Z. & HUSSAIN, A. K. M. F. 1982 The self-exited axisymmetric jet. *J. Fluid Mech.* **115**, 59–89.

KELLER, J. J. 1994 On tornado-like vortex flows. *Phys Fluids* **6**, 1524–1534.

KHORAMI, M. R. & TRIVELI, P. 1994 The viscous stability analysis of Long's vortex. *Phys. Fluids* **6**, 2623–2630.

LANDAU, L. D. 1944 On exact solution of the Navier–Stokes equations. *Dokl. Akad. Nauk SSSR* **43**, 299–301.

LEIBOVICH, S. 1984 Vortex stability and breakdown: survey and extension. *AIAA J.* **22**, 1192–1206.

LONG, R. R. 1961 A vortex in an infinite viscous fluid. *J. Fluid Mech.* **11**, 611–623.

LOPEZ, J. M. 1994 On the bifurcation structure of axisymmetric vortex breakdown in a constricted pipe. *Phys. Fluids* **6**, 3683–3693.

MORTON, B. R. 1969 The strength of vortex and swirling core flows. *J. Fluid Mech.* **38**, 315–333.

PAULL, R. & PILLOW, A. F. 1985 Conically similar viscous flows. Part 3. Characterization of axial causes of swirling flows and one-parameter flow generated by a uniform half-line source of kinematic swirl angular momentum. *J. Fluid Mech.* **155**, 359–380.

PECKHAM, D. H. & ATKINSON, S. A. 1957 Preliminary results of low speed wind tunnel tests on a Gothic wing of aspect ratio 1.0. *Aero. Res. Counc. Tech. Rep. CP-508, TN NO. Aero. 2504.*

SAFFMAN, P. G. 1992 *Vortex Dynamics*. Cambridge University Press.

SCHLICHTING, H. 1933 Laminaire Strahlausbreitung. *Z. Angew. Math. Mech.* **13**, 260–263.

SCHLICHTING, H. 1979 *Boundary-Layer Theory*. McGraw-Hill.

SCHMUKER, A. & GERSTEN, K. 1988 Vortex breakdown and its control on delta wings. *Fluid Dyn. Res.* **3**, 268–272.

SCHNEIDER, W. 1985 Decay of momentum flux in submerged jets. *J. Fluid Mech.* **154**, 91–110.

SCHNEIDER, W., ZAUNER, E. & BOHM, H. 1987 The recirculatory flow induced by a laminar axisymmetric jet issuing from a wall. *Trans. ASME* I: *J. Fluids Engng* **109**, 237–241.

SERRIN, J. 1972 The swirling vortex. *Phil. Trans. R. Soc. Lond.* A **271**, 325–360.

SHTERN, V. & HUSSAIN, F. 1993 Hysteresis in a swirling jet as a model tornado. *Phys. Fluids* A **5**, 2183–2195 (referred to herein as SH).

SLEZKIN, N. A. 1934 On a case of integrability of the full differential equations of viscous fluid motion. *Sci. Pap. Moscow Univ.* **2**, 89–90.

SNOW, J. T. 1982 A review of recent advances in tornado vortex dynamics. *Rev. Geophys. Space Phys.* **20**, 953–964.

SOZOU, C. 1992 On solution relating to conical vortices over a plane wall. *J. Fluid Mech.* **244**, 633–644.

SOZOU, C., WILKINSON, L. C. & SHTERN, V. 1994 On swirling flows in infinite fluid. *J. Fluid Mech.* **276**, 261–271.

SPOTAR', S. YU., CHOHAR', I. A., LUKASHOV, V. V. & PROZOROV, D. S. 1994 A method and device for vortex suction of gases. Proposal N 5050257, approved 1.06.1994.

SPOTAR', S. YU. & TEREKHOV, V. I. 1987 Two spontaneously alternating regimes of a vortex flow above a plane. *J. Appl. Mech. Tech. Phys.* No. 2, 68–70.

SQUIRE, H. B. 1952 Some viscous fluid flow problems. 1. Jet emerging from a hole in a plane wall. *Phil. Mag.* **43**, 942–945.

SQUIRE, H. B. 1956 Rotating fluids. In *Surveys in Mechanics* (ed. by G. K. Batchelor & R. M. Davies), pp. 139–161. Cambridge University Press.

STUART, J. T. 1987 A critical review of vortex breakdown theory. *Proc. 2nd Intl Colloq. Vortical Flows*, pp. 1–23. Switzerland, Brown Bovery Company.

YIH, C.-S., WU, F., GARG, A. K. & LEIBOVICH, S. 1982 Conical vortices: A class of exact solutions of the Navier–Stokes equations. *Phys. Fluids* **25**, 2147–2157.